JM PAPERS

Influence of parametric forcing on Marangoni instability

I.B. Ignatius[1],†, B. Dinesh[2], G.F. Dietze[3] and R. Narayanan[1]

[1]Department of Chemical Engineering, University of Florida, Gainesville, FL 32611, USA

[2]Department of Chemical Engineering and Technology, Indian Institute of Technology-BHU, Varanasi, UP 221005, India

[3]Université Paris-Saclay, CNRS, FAST, Orsay 91405, France

We study a thin, laterally confined heated liquid layer subjected to mechanical parametric forcing without gravity. In the absence of parametric forcing, the liquid layer exhibits the Marangoni instability, provided the temperature difference across the layer exceeds a threshold. This threshold varies with the perturbation wavenumber, according to a curve with two minima, which correspond to long- and short-wave instability modes. The most unstable mode depends on the lateral confinement of the liquid layer. In wide containers, the long-wave mode is typically observed, and this can lead to the formation of dry spots. We focus on this mode, as the short-wave mode is found to be unaffected by parametric forcing. We use linear stability analysis and nonlinear computations based on a reduced-order model to investigate how parametric forcing can prevent the formation of dry spots. At low forcing frequencies, the liquid film can be rendered linearly stable within a finite range of forcing amplitudes, which decreases with increasing frequency and ultimately disappears at a cutoff frequency. Outside this range, the flow becomes unstable to either the Marangoni instability (for small amplitudes) or the Faraday instability (for large amplitudes). At high frequencies, beyond the cutoff frequency, linear stabilization through parametric forcing is not possible. However, a nonlinear saturation mechanism, occurring at forcing amplitudes below the Faraday instability threshold, can greatly reduce the film surface deformation and therefore prevent dry spots. Although dry spots can also be avoided at larger forcing amplitudes, this comes at the expense of generating large-amplitude Faraday waves.

Key words: Marangoni convection, thin films, Faraday waves

† Email address for correspondence: iginbenny@gmail.com

981 A8-1

I.B. Ignatius, B. Dinesh, G.F. Dietze and R. Narayanan

1. Introduction

A fluid system with a free surface, when heated from below and subjected to vertical periodic oscillations, can give rise to flow due to either thermal convective instabilities from the imposed temperature gradients or resonant instability from the external periodic forcing. Thermal convective instabilities are either buoyancy-driven, occurring in thick layers, or surface tension gradient-driven, occurring in thin layers (thinner than the capillary length) or in microgravity (Sarma 1987). In this work, we limit ourselves to surface tension gradient-driven instability, also known as Marangoni instability, assuming that there are no density variations, gravity is absent (Grodzka & Bannister 1972; Kamotani, Ostrach & Pline 1995) and that there is no phase change at the interface.

The Marangoni instability is driven by a perturbation in surface temperature when a liquid film with a free surface is heated from the liquid side. The resulting surface tension variation, assuming that surface tension decreases with increasing temperature, drives flow against the stabilizing effects of viscosity and thermal diffusivity (Pearson 1958; Koschmieder 1993). The threshold of the Marangoni instability, expressed via the critical temperature difference as a function of the wavenumber, exhibits two minima in the absence of gravity (Scriven & Sternling 1964). These minima are associated with long-wave and short-wave instability modes. The short-wave instability mode, which is characterized by a weak interface deformation, emerges when the container width is of the order of the fluid depth. Conversely, the long-wave mode, which is associated with a strong interface deformation, emerges when the depth is small compared with the container width (Scriven & Sternling 1964; Davis 1987). In that case, the instability is subcritical, leading to an unbounded growth of the surface deformation, and eventually, film rupture and dry spot formation. This was demonstrated in the experiments of Vanhook *et al.* (1997), who used very thin liquid layers of thickness ~ 0.1 mm, as well as nonlinear computations based on low-dimensional long-wave models (Oron, Davis & Bankoff 1997; Vanhook *et al.* 1997). Avoiding dry spot formation is important for several thin film applications where surface defects need to be prevented, such as coating processes (Yiantsios & Higgins 2006), additive manufacturing under microgravity conditions (Lee & Farson 2016) and in thin film microgravity heat pipes (Alexeev, Gambaryan-Roisman & Stephan 2005; Ajaev 2013), where both evaporative and Marangoni effects play a role.

It is known that external forcing can be used to stabilize a dynamical system, as seen in the simple example of an inverted pendulum with an oscillating anchor point (Stephenson 1908). Several works have applied this idea to different instabilities arising in hydrodynamical systems, e.g. Rayleigh–Bénard (Gresho & Sani 1970; Shukla & Narayanan 2002), Taylor–Couette (Murray, McFadden & & Coriell 1990), Rayleigh–Taylor (Sterman-Cohen, Bestehorn & Oron 2017), Plateau–Rayleigh (Halpern & Grotberg 2003; Haimovich & Oron 2010) and Kapitza (Gottlieb & Oron 2004) instabilities. At the same time, external forcing applied to a liquid layer can lead to resonance-driven instability, known as Faraday instability (Faraday 1831). For the configuration considered here, i.e. a thin liquid film subject to the Marangoni instability, this poses an optimization challenge, which we aim to resolve: to tune the external forcing such as to quench the Marangoni instability, without triggering the Faraday instability. In particular, we aim to identify the critical parameter range and the mechanisms through which periodic forcing can stave off dry spot formation. We commence by placing our work in the context of past studies on this subject, all of which have considered laterally unconfined layers.

Briskman (1996) and Skarda (2001) studied the effect of g-jitter on the Marangoni instability by applying periodic forcing to a liquid layer with a non-deformable interface and temperature-dependent density. These authors concluded that the critical Marangoni

number increases with the so-called vibrational Rayleigh number, which accounts for the acceleration induced by periodic forcing. This may be contrasted with the classical result for Bénard instability in a steady gravitational field, where the critical Marangoni number decreases with increasing Rayleigh number (Nield 1964). In the same paper, experiments were performed by Briskman (1996), where high frequency vibrations were used to stave off the formation of dry spots.

Nepomnyashchy & Simanovskii (2010, 2013) and Fayzrakhmanova & Nepomnyashchy (2018) used long-wave models based on the lubrication approximation, i.e. where inertia is ignored, to study the influence of mechanical oscillations on a trilayer system consisting of two liquids superposed by a passive gas layer unstable on account of the Marangoni effect. They found two stability bounds for the Marangoni number as a function of the perturbation wavenumber, using linear stability analysis. The onset of Marangoni instability was given by the first stability bound while the system reverted to its stable state when heated beyond the second critical threshold. The region of instability between these two critical Marangoni numbers was found to diminish with the application of periodic forcing, i.e. the system was stabilized. Nonlinear computations based on this model demonstrated the formation of two-dimensional and three-dimensional oscillatory surface patterns at large forcing amplitudes.

The works of Thiele, Vega & Knobloch (2006) and Shklyaev, Alabuzhev & Khenner (2015) are particularly relevant to our current study, notwithstanding that gravity was taken into account in these works. In both studies, the authors employed a long-wave model based on the lubrication approximation to investigate the linear and nonlinear effects of Faraday forcing on the Marangoni instability. Thiele *et al.* (2006) showed that the neutral stability bound of the Marangoni instability can be raised via periodic forcing when the forcing frequency is large. The resulting region of stability, which is bounded at large amplitudes by the Faraday instability threshold, increases in width as the forcing frequency is increased. The study went on to consider the nonlinear dynamics of the liquid film for parameters chosen such that the film is unstable in the absence of forcing. In that limit, which corresponds to the pure Marangoni instability, the authors obtained steady solutions in the shape of drops separated by dry zones, and showed that these could be forced to revert back to a flat-film state upon applying mechanical vibrations, thereby preventing the formation of dry spots.

Shklyaev *et al.* (2015) focused on lower frequencies compared with Thiele *et al.* (2006) and showed that the critical Marangoni number increases with increasing vibrational amplitude also in this range. For the forcing amplitudes investigated, the authors further showed that the nature of the bifurcation underlying the long-wave Marangoni instability mode remains subcritical in the presence of periodic forcing.

The current work distinguishes itself from those of Thiele *et al.* (2006) and Shklyaev *et al.* (2015) in several important ways. First, our linear and nonlinear models account for inertia in the momentum and energy equations, which is known to play an important role in systems involving resonant forcing. Second, we include the effects of finite container width, thereby restricting ourselves to experimentally allowable disturbance wavenumbers. Third, linear stability calculations are based on the full governing equations without invoking a long-wave approximation. As a result of these distinctions, we have made several new observations. In particular, we find that the amplitude range of the stable region, where periodic forcing can suppress the Marangoni instability without triggering the Faraday instability, decreases with increasing forcing frequency, which is opposite to the trend predicted by Thiele *et al.* (2006). Moreover, beyond a critical forcing frequency, the neutral bound of the Faraday instability moves below that of the Marangoni instability, thus making it impossible to suppress flow via a linear mechanism. Nonetheless,
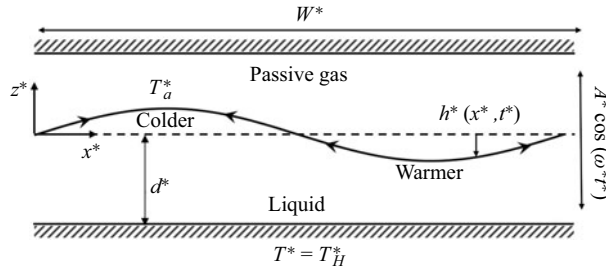
Figure 1. Schematic of the studied configuration. A liquid layer is subject to the Marangoni instability and a mechanical oscillation in the z-direction, in the absence of gravity. The liquid is heated via a bottom wall at fixed temperature T_H^* and cooled via the ambient (hydrodynamically passive) gas at a temperature $T_a^* < T_H^*$. Arrows at the interface indicate the flow direction due to temperature-driven surface tension gradients.

we identify a nonlinear saturation mechanism in that frequency range, which prevents the formation of dry spots. By contrast, we find that the effect of parametric forcing on the short-wave mode of the Marangoni instability is very weak. Finally, the reduced-order model used for our nonlinear calculations extends the state of the art by accounting for both the Marangoni and Faraday instabilities.

The manuscript is arranged as follows. In § 2, we introduce the mathematical model governing the fluid system considered (figure 1). In § 3, we discuss the effect of parametric forcing on the long- and short-wave modes of the Marangoni instability, via linear stability calculations. In § 4, we develop a reduced-order long-wave model using the weighted residual integral boundary layer (WRIBL) technique (Ruyer-Quil & Manneville 2000) and employ it to perform transient computations of the nonlinear evolution of the liquid film in different stability regimes. As a result, we arrive at two mechanisms by which the formation of Marangoni-induced dry spots can be suppressed via periodic forcing.

2. Mathematical model

Our physical system is sketched in figure 1, where all dimensioned variables are denoted with an asterisk. We consider a Newtonian liquid layer of unperturbed height, d^*, heated by a lower wall of fixed temperature, T_H^*, and subjected to a mechanical oscillation of angular frequency, ω^*, and amplitude, A^*, in the z-direction in the absence of gravity. The gas above the free surface of the liquid layer is taken to be hydrodynamically passive and cooled by an upper wall. The gas layer is maintained at a temperature $T_a^* < T_H^*$, so that the liquid is cooled via the free surface according to Newton's law of cooling. The effect of a hydrodynamically active air layer is discussed in Appendix B.

The density, ρ, viscosity, μ, thermal conductivity, λ, and heat capacity , C_p, of the liquid are assumed constant, whereas its surface tension, γ, varies linearly with temperature at the free surface as

$$\gamma = \gamma_0 - \gamma_T(T^* - T_0^*), \tag{2.1}$$

where the subscript 0 refers to the unperturbed base state and γ_0 denotes the surface tension at the corresponding free surface temperature, $T_0^*|_{z=0}$. Further, we assume $\gamma_T > 0$.

2.1. *Nonlinear equations*

The fluid motion is governed by the continuity and Navier–Stokes equations while the temperature field of the system is governed by the energy equation, i.e.

$$\nabla^* \cdot v^* = 0, \tag{2.2}$$

$$\rho \left(\frac{\partial v^*}{\partial t^*} + v^* \cdot \nabla^* v^* \right) = -\nabla^* p^* + \mu \nabla^{*2} v^* - \rho (A^* \omega^{*2} \cos(\omega^* t^*)) e_z \tag{2.3}$$

and

$$\rho C_p \left(\frac{\partial T^*}{\partial t^*} + v^* \cdot \nabla^* T^* \right) = \lambda \nabla^{*2} T^*. \tag{2.4}$$

In (2.2)–(2.4), e_z is the unit vector along the z direction. Here, A^* and ω^* are the amplitude and the angular frequency of the parametric forcing.

At the bottom wall, $z^* = -d^*$, we impose no-slip and no-penetration conditions for velocity and a Dirichlet condition for temperature i.e.

$$v^* = 0 \quad \text{and} \quad T^* = T_H^*. \tag{2.5a,b}$$

At the impenetrable interface, $z^* = h^*(x^*, t^*)$, the jump mass balance yields

$$(v^* - u^*) \cdot n^* = 0, \tag{2.6}$$

for which the interface velocity vector, u^*, the unit normal, n^*, and unit tangent vectors, t^*, are given by

$$u^* \cdot n^* = \frac{\dfrac{\partial h^*}{\partial t^*}}{\left(1 + \left(\dfrac{\partial h^*}{\partial x^*}\right)^2\right)^{1/2}}, \quad n^* = \frac{-\dfrac{\partial h^*}{\partial x^*} e_x + e_z}{\left(1 + \left(\dfrac{\partial h^*}{\partial x^*}\right)^2\right)^{1/2}}, \quad t^* = \frac{e_x + \dfrac{\partial h^*}{\partial x^*} e_z}{\left(1 + \left(\dfrac{\partial h^*}{\partial x^*}\right)^2\right)^{1/2}}. \tag{2.7a–c}$$

The fluid loses heat from the free surface through a purely conducting gas layer via Newton's law of cooling, i.e.

$$\mathcal{H}(T^* - T_a^*) = -\lambda \nabla^* T^* \cdot n^*, \tag{2.8}$$

where the heat transfer coefficient is defined via $\mathcal{H} = \lambda_a / d_a^*$, with λ_a and d_a^* being the thermal conductivity and height of the gas layer. The force balance at the interface is

$$n^* \cdot \mathcal{T}^* + \gamma n^* \nabla^* \cdot n^* - \nabla_s^* \gamma = 0, \tag{2.9}$$

where, the stress tensor $\mathcal{T}^*$ is given by $\mathcal{T}^* = -p^* I + \mu (\nabla^* v^* + \nabla^* v^{*T})$. Here ∇_s^* is the surface gradient operator and is given by $\nabla^* - n^*(n^* \cdot \nabla^*)$. We now turn our focus to obtaining the non-dimensional governing equations.

2.2. *Non-dimensional equations*

The following characteristic scales are used to obtain non-dimensionalized variables:

$$
\left.
\begin{aligned}
&x = \frac{x^*}{W^*}, \quad z = \frac{z^*}{d^*}, \quad u = \frac{u^*}{U}, \quad w = \epsilon\frac{w^*}{U}, \quad t = \frac{t^*}{\left(\dfrac{d^*}{\epsilon U}\right)}, \\
&\omega = \omega^*\left(\frac{d^*}{\epsilon U}\right), \quad p = \frac{p^*}{\left(\dfrac{\mu U}{d^*}\right)} \quad \text{and} \quad T = \frac{T^* - T_{i0}^*}{\Delta T^*},
\end{aligned}
\right\}
\tag{2.10}
$$

where $U = \kappa/d^*$ is a characteristic horizontal velocity based on the time scale for thermal diffusion, $\kappa = \lambda/\rho C_p$ is the thermal diffusivity and $\Delta T^* = T_H^* - T_{i0}^*$ is the temperature difference across the unperturbed fluid layer.

Observe that we render x and z dimensionless using W^* and d^*, respectively. This leads to a length scale separation parameter, ϵ, given by $\epsilon = d^*/W^*$, which will play a role when we consider the long-wave limit of the problem in § 4. Upon non-dimensionalizing equations (2.2)–(2.9) we get

$$
\frac{\partial u}{\partial x} + \frac{\partial w}{\partial z} = 0,
\tag{2.11}
$$

$$
\epsilon Re\left(\frac{\partial u}{\partial t} + u\frac{\partial u}{\partial x} + w\frac{\partial u}{\partial z}\right) = -\epsilon\frac{\partial p}{\partial x} + \epsilon^2\frac{\partial^2 u}{\partial x^2} + \frac{\partial^2 u}{\partial z^2},
\tag{2.12}
$$

$$
\epsilon^3 Re\left(\frac{\partial w}{\partial t} + u\frac{\partial w}{\partial x} + w\frac{\partial w}{\partial z}\right) = -\epsilon\frac{\partial p}{\partial z} + \epsilon^4\frac{\partial^2 w}{\partial x^2} + \epsilon^2\frac{\partial^2 w}{\partial z^2} - \epsilon\mathcal{A}\cos(\omega t)
\tag{2.13}
$$

and

$$
\epsilon\left(\frac{\partial T}{\partial t} + u\frac{\partial T}{\partial x} + w\frac{\partial T}{\partial z}\right) = \epsilon^2\frac{\partial^2 T}{\partial x^2} + \frac{\partial^2 T}{\partial z^2},
\tag{2.14}
$$

where $Re = \rho U d^*/\mu$ is the Reynolds number and $\mathcal{A} = \rho A^*\omega^{*2}d^{*2}/\mu U$. The scaled boundary conditions at the bottom wall, $z = -1$, are

$$
u = 0, \quad w = 0 \quad \text{and} \quad T = 1.
\tag{2.15a–c}
$$

The non-dimensional form of the mass balance at the impenetrable interface, $z = h(x, t)$, along with the tangential and normal force balance conditions are

$$
\epsilon w - \epsilon u\frac{\partial h}{\partial x} = \epsilon\frac{\partial h}{\partial t},
\tag{2.16}
$$

$$
\left(\frac{\partial u}{\partial z} + \epsilon^2\frac{\partial w}{\partial x}\right)\left(1 - \epsilon^2\left(\frac{\partial h}{\partial x}\right)^2\right) + 4\epsilon^2\frac{\partial w}{\partial z}\frac{\partial h}{\partial x}
$$

$$
= -\epsilon Ma\left(\frac{\partial T}{\partial x} + \frac{\partial T}{\partial z}\frac{\partial h}{\partial x}\right)\left[1 + \epsilon^2\left(\frac{\partial h}{\partial x}\right)^2\right]^{1/2}
\tag{2.17}
$$

and

$$-\epsilon p + 2\epsilon^2 \left[\frac{\partial w}{\partial z} \left(1 - \epsilon^2 \left(\frac{\partial h}{\partial x} \right)^2 \right) - \left(\frac{\partial u}{\partial z} + \epsilon^2 \frac{\partial w}{\partial x} \right) \left(\frac{\partial h}{\partial x} \right) \right] \left[1 + \epsilon^2 \left(\frac{\partial h}{\partial x} \right)^2 \right]^{-1}$$

$$= \epsilon^3 \left(\frac{1}{Ca} - MaT \right) \frac{\partial^2 h}{\partial x^2} \left[1 + \epsilon^2 \left(\frac{\partial h}{\partial x} \right)^2 \right]^{-3/2}, \tag{2.18}$$

where $Ca = \mu U / \gamma$ and $Ma = \gamma_T \Delta T^* / \mu U$ are the capillary and Marangoni numbers, respectively. Newton's law of cooling at the free surface becomes

$$Bi(T - T_a) + \left(\frac{\partial T}{\partial z} - \epsilon^2 \frac{\partial T}{\partial x} \frac{\partial h}{\partial x} \right) \left[1 + \epsilon^2 \left(\frac{\partial h}{\partial x} \right)^2 \right]^{-1/2} = 0, \tag{2.19}$$

where $T_a = (T_a^* - T_{io}^*)/(T_H^* - T_{io}^*)$ and where $Bi = \mathcal{H} d^* / \lambda$ is the Biot number.

In what follows we shall consider the nonlinear (2.11)–(2.19) in different limits. In § 3, we discuss the stability analysis for arbitrary wavenumbers by choosing d^* to be the common length scale for the horizontal and vertical directions. This amounts to setting $\epsilon = 1$ without any loss of generality. By contrast, in § 4, we will retain the original scaling and consider the limit $\epsilon \ll 1$.

3. Linear stability analysis of the finite wave model

The scaled governing equations (2.11)–(2.19) are linearized around the quiescent and purely conductive base state (subscript 0) given by

$$u_0 = w_0 = h_0 = 0, \quad \frac{dp_0}{dz} = -\mathcal{A} \cos(\omega t) \quad \text{and} \quad \frac{dT_0}{dz} = -1, \tag{3.1a--c}$$

by introducing Floquet expansions (Nayfeh 1981). Thus, we have

$$h(x, t) = h_0 + h'(x, t) = h_0 + e^{ikx + \sigma t} \sum_{n=-N}^{N} \hat{h}_n \, e^{(in\omega/2)t}, \tag{3.2a}$$

and $$\Psi(x, z, t) = \Psi_0(z) + \Psi'(x, z, t) = \Psi_0(z) + e^{ikx + \sigma t} \sum_{n=-N}^{N} \hat{\Psi}_n(z) \, e^{(in\omega/2)t}, \tag{3.2b}$$

where $\Psi = u, v, p$ and T, where primes denote infinitesimal perturbations, and where hats denote perturbation amplitudes. Here, $k \in \mathbb{R}$, $\sigma \in \mathbb{C}$ and $\omega \in \mathbb{R}$ denote the wavenumber, complex linear frequency and parametric frequency, respectively. For a fixed container width, W, and periodic conditions, the wavenumber is limited to discrete values $k = m2\pi/W$, with $m \in \mathbb{N}$. The summations in (3.2) are Floquet series that ensure compatibility with the harmonic forcing term in the z-momentum equation (2.13). Here, N sets the number of oscillatory modes considered.

Upon substitution of the forms given by (3.1a–c) and (3.2), the linearized equations (dropping the subscript, *n*, in the (3.3)–(3.9), and (3.11)) (2.11)–(2.19), become

$$ik\hat{u} + \frac{\partial \hat{w}}{\partial z} = 0, \tag{3.3}$$

$$Re\hat{u}\left(\sigma + \frac{in\omega}{2}\right) = -ik\hat{p} - k^2\hat{u} + \frac{\partial^2 \hat{u}}{\partial z^2}, \tag{3.4}$$

$$Re\hat{w}\left(\sigma + \frac{in\omega}{2}\right) = -\frac{\partial \hat{p}}{\partial z} - k^2\hat{w} + \frac{\partial^2 \hat{w}}{\partial z^2} \tag{3.5}$$

and

$$\hat{T}\left(\sigma + \frac{in\omega}{2}\right) - \hat{w} = -k^2\hat{T} + \frac{\partial^2 \hat{T}}{\partial z^2}. \tag{3.6}$$

The linearized boundary conditions at the bottom wall, $z = -1$, are

$$\hat{u} = 0, \quad \hat{w} = 0 \quad \text{and} \quad \hat{T} = 0. \tag{3.7a–c}$$

The linearized boundary conditions at the interface, $z = 0$, are

$$\hat{w} = \left(\sigma + \frac{in\omega}{2}\right)\hat{h}, \tag{3.8}$$

$$\frac{\partial \hat{u}}{\partial z} + ik\hat{w} = -ikMa(\hat{T} - \hat{h}), \tag{3.9}$$

$$\sum_{n=-N}^{n=N} e^{(in\omega/2)t}\left\{-\hat{p}_n + \mathcal{A}\hat{h}_n\frac{\left(e^{i\omega t} + e^{-i\omega t}\right)}{2} + 2\frac{\partial \hat{w}_n}{\partial z} = -k^2\frac{1}{Ca}\hat{h}_n\right\} \tag{3.10}$$

and

$$Bi(\hat{T} - \hat{h}) + \frac{\partial \hat{T}}{\partial z} = 0. \tag{3.11}$$

We now express $\hat{\Psi}_n(z)$ via polynomials of order N_z and evaluate the domain equations at the corresponding Chebyshev Gauss–Lobatto collocation points (Guo, Labrosse & Narayanan 2013). This is done for all $n \in [-N, N]$, yielding an $(N_z + 1)(2N + 1) \times (N_z + 1)(2N + 1)$ generalized eigenvalue problem of the form

$$Ax = \sigma Bx, \tag{3.12}$$

with eigenvalue $\sigma = \sigma_r + i\sigma_i$ and the eigenvector x. Here, σ_r is the temporal growth rate and σ_i is the corresponding linear frequency shift with respect to the forcing frequency, ω. The system (3.12) is solved numerically for σ at given values of ω, k, $\mathcal{A}$ and Ma, using the Eigenvalues routine in Mathematica. The neutral stability bounds, i.e. $\sigma_r = 0$, are obtained by finding a set of input parameters, say, $\mathcal{A}$ and Ma, for assigned values of ω and k. For example, to determine the critical Marangoni number, we fix the values of ω, k and $\mathcal{A}$ and increment the Marangoni number until it reaches a critical value, where σ_r becomes zero. Likewise, the threshold for the forcing amplitude, is determined by changing the forcing amplitude until σ_r becomes zero for fixed values of ω, k and Ma. Numerical calculations performed in this study show that at these critical values, one of the eigenvalues, $(\sigma_r, \sigma_i) = (0, 0)$, implying exchange of stability at the neutral point.

Physical property	Symbol	Value
Density	ρ	935 kg m^{-3}
Viscosity	μ	0.01 Pa s
Surface tension	γ	0.02 N m^{-1}
Thermal conductivity	λ	0.134 W m^{-1} K^{-1}
Specific heat	Cp	1507 J kg^{-1} K^{-1}
Film thickness	d^*	3×10^{-3} m

Table 1. Physical properties used in the calculations. Fluid properties correspond to silicone oil (XIAMETER™ PMX-200).

The nature of the temporal response of the interface associated with a given eigenvalue, σ, is determined by examining the perturbation amplitudes, $\hat{h}_n$, in the Floquet summation. Note that the response of the interface deformation is harmonic if the odd coefficients in the Floquet summation are zero, the even coefficients are non-zero and the coefficient corresponding to $n = \pm 2$ has the dominant magnitude amongst all even coefficients. On the other hand, if the coefficient corresponding to $n = \pm 4$ is dominant then the response is twice harmonic. Likewise the response of the interface deformation is subharmonic if the even coefficients are zero and the odd coefficients are non-zero with the coefficients corresponding to $n = \pm 1$ having a dominating magnitude etc. If the dominant coefficient corresponds to $n = 0$ then we consider the response to be principally steady. The temporal behaviour of the interface deflections will be useful in understanding the stability diagrams in our calculations. To distinguish the two types of temporal responses in the case of instability ($\sigma_r > 0$), we will call the mode 'monotonic' when $n = 0$ is dominant and 'oscillatory' when $n \neq 0$ is dominant.

In the following subsections, we present results of linear stability calculations for a set of representative parameters, given in table 1, where the fluid properties correspond to a definite fluid system of film thickness, d^*, and container width, W^*, based on practical considerations. The stability results are arranged as follows. We first review the results from the pure Marangoni problem, then those from the pure Faraday problem followed by the combined problem. Here we shall focus on the role of the finiteness of the container width, a feature that will be important in the interpretation of the key results in this study. We then conclude the section by considering the problem from the perspective of parametric forcing on an erstwhile unstable layer due to the Marangoni effect.

3.1. *Pure Marangoni instability*

The linear stability calculation for the pure Marangoni problem, done for the parameters given in tables 1 and 2, is depicted in figures 2(*a*) and 2(*b*) as plots of critical Marangoni number versus the wavenumber. The initial rise and fall in the curves are due to the competition between the stabilizing effect of surface tension and the destabilizing effect of surface tension gradients. This is followed by a final rise due to stabilization afforded by viscosity and thermal diffusion. Due to the finiteness of the horizontal extent of the container, the allowable wavenumbers, k, are given by $k = 2m\pi/W$, where $m \in \mathbb{N}$ and W is the dimensionless width, i.e. W^*/d^*. For example, when $1/W = 0.075$, the allowable wavenumbers are depicted by the vertical lines drawn in figure 2(*a*) i.e. at $k = 2\pi/W, 4\pi/W, 6\pi/W$, etc. Clearly, the minimum critical Marangoni number, denoted Ma_c, occurs at the wavenumber, $k = 8\pi/W$, i.e. corresponding to four full waves within

Dimensionless groups	Value
Re	10^{-2}
Ca	1.15×10^{-5}
Pr	100
Bi	0.1

Table 2. Values of dimensionless groups used in the calculations.
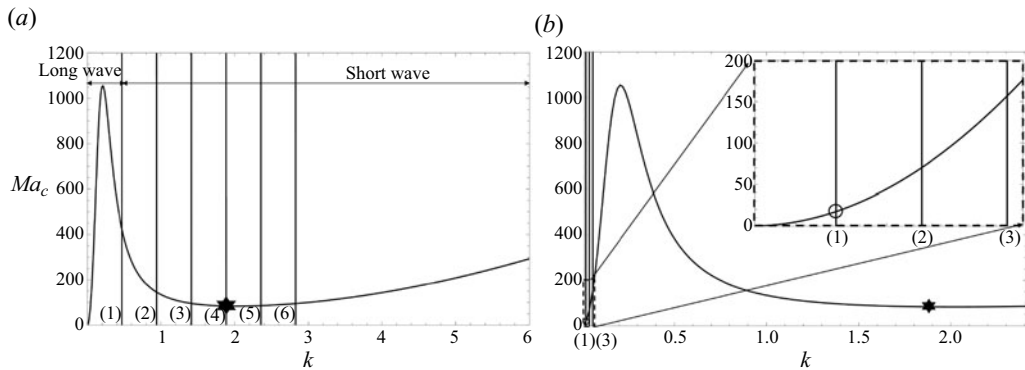
(a)

(b)

Figure 2. Critical Ma versus k curves, marking allowable wavenumbers $k = 2m\pi/W$ with vertical lines. The numbers between parentheses correspond to m. Here (a) $1/W = 0.075$ and (b) $1/W = 0.003$. The inset in (b) is a magnification of the low wavenumber range.

the container and denoted by the star in figure 2(a). However, if $1/W = 0.003$ we arrive at figure 2(b) where now the minimum critical Marangoni number occurs at $k = 2\pi/W$, i.e. corresponding to one full wave, and is lower than the short-wave critical Marangoni number depicted in figure 2(b), denoted by an asterisk.

3.2. *Pure Faraday instability*

We now turn to the second of the two primary calculations, where the critical amplitude of shaking, $\mathcal{A}$, for the onset of Faraday instability is obtained in the absence of Marangoni instability. The Faraday instability principally arises when the parametric forcing frequency is commensurate with the system's natural frequency. The natural frequency, however, depends on Ca, Re and on the wavenumber of the disturbance, k. It is determined by calculating $Im(\sigma)$ i.e. σ_i via (3.3)–(3.5) and (3.7a–c)–(3.10) modified here by taking $Ma = 0$, $\omega = 0$ and $\mathcal{A} = 0$. Now, depending on the frequency range of oscillation, the instability can give rise to different waveforms which are marked in the figures 3(a) and 3(b). The calculation is done by setting the frequency and then determining the minimum critical amplitude, denoted A_c^*, as we sweep through the allowable waveforms, say, $k = 2\pi/W$, $k = 4\pi/W$, $k = 6\pi/W$, etc. The lowest of the minimum amplitudes and the corresponding waveforms constitute the critical diagram, figure 3, displayed in terms of dimensioned quantities to emphasize the practical attainability of the results. This figure, drawn again for the two cases, i.e. $1/W = 0.075$ and $1/W = 0.003$, shows the effect of sidewall proximity. From figure 3(a) we see that there are minimum points in the frequency range where resonance is strongest for each interfacial mode. These minimum points in each of these frequency ranges are near,
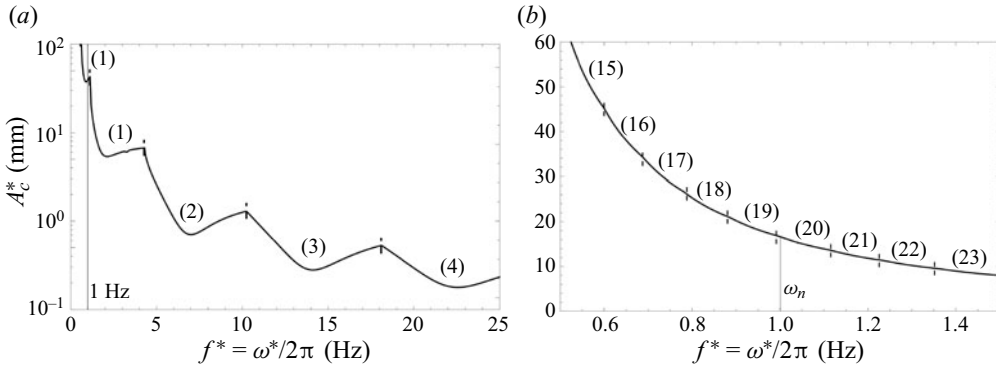
Figure 3. Critical forcing amplitude (A_c^*) versus frequency (f^*) for the pure Faraday instability. The numbers between parentheses correspond to *m*. The vertical line corresponds to $f^* = 1$ Hz. Here (*a*) $1/W = 0.075$ and (*b*) $1/W = 0.003$.

but not precisely at, the natural frequency associated with the waveforms. The critical curve is concatenated from the individual waveforms. However, this feature becomes less discernible as the dimensionless width becomes very large. We see this behaviour in figures 3(*a*) and 3(*b*), with figure 3(*b*) being drawn for a very large value of the dimensionless width compared with figure 3(*a*).

Unlike the Marangoni instability, the Faraday instability is strongly dependent on the fluid's inertia i.e. the Reynolds number, *Re*. The inertial motion acts on the deflecting interface and just as gravity acts to stabilize the long-wave Marangoni instability (Vanhook *et al.* 1997) we might expect that inertial action on the fluid interface can stave off the Marangoni instability with parametric forcing. To see if this is so we turn to the next stability calculation which shows the effect of resonance on the Marangoni instability.

3.3. *The effect of Faraday forcing on the long-wave Marangoni instability*

We now consider the effect of parametric forcing on the Marangoni instability focusing first on the long-wave regime. In this setting, there are two leading instability modes. The first mode, with critical Marangoni number Ma_s, gives rise to predominantly monotonic temporal growth beyond criticality and produces a steady response at criticality, i.e. the dominant term in the Floquet expansion is $n = 0$. The second mode, with threshold Ma_o, is predominantly oscillatory as a result of resonance. It is subharmonic in nature, i.e. the dominant term in the Floquet expansion is $n = 1$.

We first focus on mode *s*, which connects to the classical Marangoni instability mode in the absence of forcing ($\mathcal{A} = 0$). We perform stability calculations for different forcing amplitudes, $\mathcal{A}$, at fixed frequency $f^* = 1$ Hz and $1/W = 0.003$. Figure 4 represents the results of these calculations. The solid curve corresponds to the pure Marangoni instability ($\mathcal{A} = 0$) while the dashed line corresponds to $\mathcal{A} = 0.5\mathcal{A}_c$ and the dot–dashed line corresponds to $\mathcal{A} = 0.9\mathcal{A}_c$. Observe that the critical Marangoni number, Ma_s, increases with amplitude of shaking over a considerable range of wavenumbers that includes the maximum of the *Ma* versus *k* curve. The stabilization in the low wavenumber region is illustrated in figure 4(*b*), where the wavenumber $k = 2\pi/W$, corresponding to a single wave within the container width, is demarcated by a vertical solid line. Thus, the long-wave monotonic Marangoni instability mode can be strongly stabilized by parametric forcing.
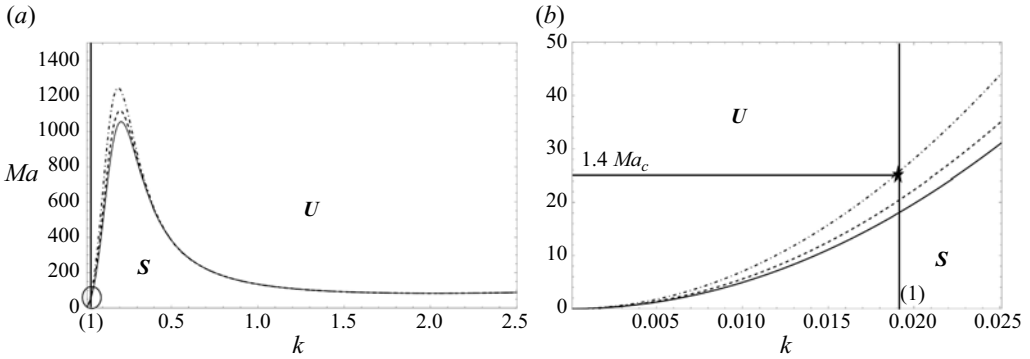
981 A8-11

Figure 4. Critical *Ma* versus *k* showing the stabilizing effect of Faraday forcing for a fixed frequency of 1 Hz. Here the amplitude of shaking is increased from $\mathcal{A} = 0$ (solid curve) to $\mathcal{A} = 0.5\mathcal{A}_c$ (dashed curve) and $\mathcal{A} = 0.9\mathcal{A}_c$ (dot–dashed curve). The corresponding critical amplitude is $A_c^* = 16.4$ mm and is marked by the vertical line in figure 3(*b*) ($1/W = 0.003$). Here *S* represents the stable region and *U* represents the unstable region.
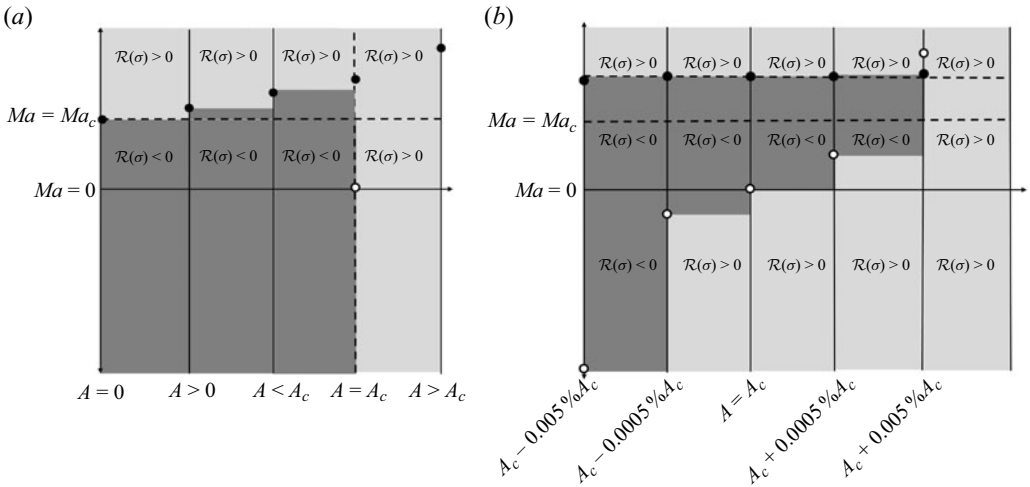

Figure 5. Stability diagrams depicting the emergence of a second instability mode for a fixed frequency, $f^* = 1$ Hz. Critical Marangoni numbers versus forcing amplitude, $\mathcal{A}$, are shown along with the sign of the real part of σ, $\mathcal{R}(\sigma)$, for the long-wave regime. The symbol ● represents Ma_s and the symbol ○ represents Ma_o. Panel (*b*) is the magnification of (*a*) in the vicinity of $\mathcal{A}_c$. The dark region represents $\mathcal{R}(\sigma) < 0$ and the light region represents $\mathcal{R}(\sigma) > 0$.

To understand what happens when $\mathcal{A} > \mathcal{A}_c$ we turn to figure 5, which represents the corresponding stability diagram. While the Ma_s are obtained for $k = 2\pi/W$, the most unstable possible wavenumber for the container width chosen, the Ma_o are obtained for $k = 40\pi/W$, the lowest wavenumber at which oscillatory modes first appear, as seen from figure 3(*b*). The dark and light grey regions indicate stable and unstable regimes which are identified based on the real part of σ, for the two leading eigenvalues. Observe that as $\mathcal{A}$ increases, Ma_s (shown by the solid dots in figure 5*a*) increases, which is in accordance with figure 4. The second instability mode, Ma_o, represented by the open circles in the magnified view shown in figure 5(*b*), appears in the proximity of $\mathcal{A}_c$. For $\mathcal{A} < \mathcal{A}_c$, Ma_o rapidly approaches negative infinity as $\mathcal{A}$ is reduced. When $\mathcal{A} = \mathcal{A}_c$, Ma_o reaches zero while Ma_s continues to increase, but at a slower rate. As a result, when $\mathcal{A} > \mathcal{A}_c$, Ma_o
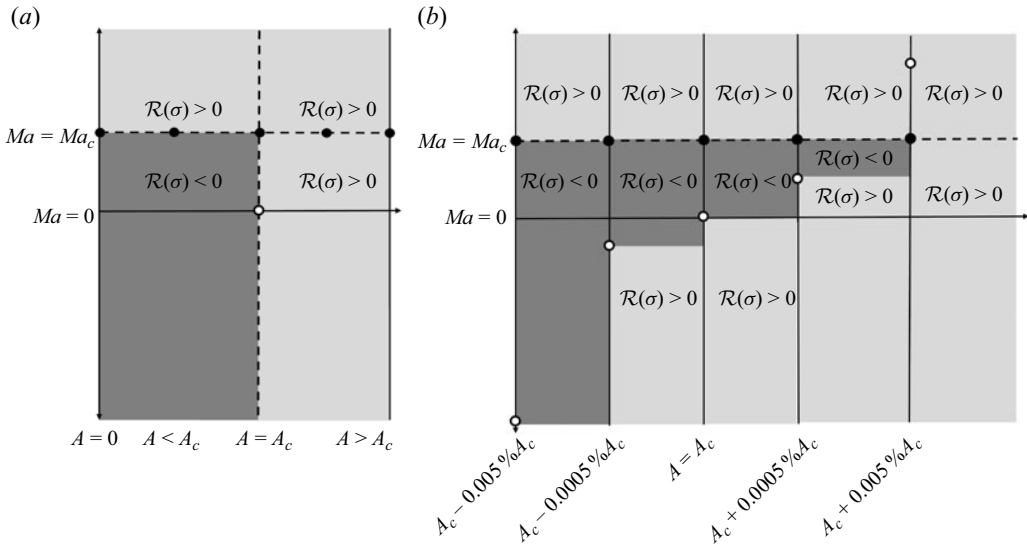
981 A8-12

Figure 6. Illustration of Ma versus $\mathcal{A}$ depicting the sign of the real part of σ, $\mathcal{R}(\sigma)$ for the short-wave regime. The symbol ● represents Ma_s and the symbol ○ represents Ma_o. The dark region represents $\mathcal{R}(\sigma) < 0$ and the light region represents $\mathcal{R}(\sigma) > 0$.

can overtake Ma_s. It is clear from figures 5(a) and 5(b) that when $Ma < Ma_o$ the flow is oscillatory but if $Ma > Ma_s$ the flow is monotonic. Clearly, if $Ma_o < Ma_s$, then the system is stable for $Ma_o < Ma < Ma_s$ and if $Ma_o > Ma_s$, then the system is always unstable.

We now turn to the task of analysing the effect of Faraday forcing on the short-wave regime.

3.4. *Effect of Faraday forcing on the short-wave Marangoni instability*

To access the short-wave Marangoni instability we consider, as an example, $1/W = 0.075$ and refer to figure 2(a), where the star locates the onset of short-wave instability and corresponds to $k = 8\pi/W$. Figure 4(a), although drawn for a wider container, suggests that the effect of forcing on the short-wave Marangoni instability is negligible. Let us verify whether this holds for the current container width, where the short-wave instability is dominant. As in the discussion of the long-wave case, figure 6 represents the corresponding stability diagram. To make a consistent comparison with the long-wave case, illustrations are shown for the same frequency, i.e. $f^* = 1$ Hz. Unlike the long-wave case, the Ma_s are obtained for $k = 8\pi/W$ (marked by a star in figure 2a) and the Ma_o are obtained for $k = 2\pi/W$ (marked by the vertical line in figure 3a), i.e. the most unstable mode for each instability type.

Observe from figures 6(a) and 6(b) that Ma_s is not affected by parametric forcing, unlike the long-wave case, while Ma_o displays the same behaviour as seen in figure 5. We thus focus on the effect of parametric forcing on the long-wave instability mode in the remainder of the manuscript.

3.5. *A practical perspective: the effect of increasing forcing amplitude at fixed Marangoni number where $Ma > Ma_c$*

In § 3.3, we saw that raising the forcing amplitude, $\mathcal{A}$, increases the threshold Marangoni number, Ma_s, in the long-wave region. This implies that an increase in $\mathcal{A}$ at fixed
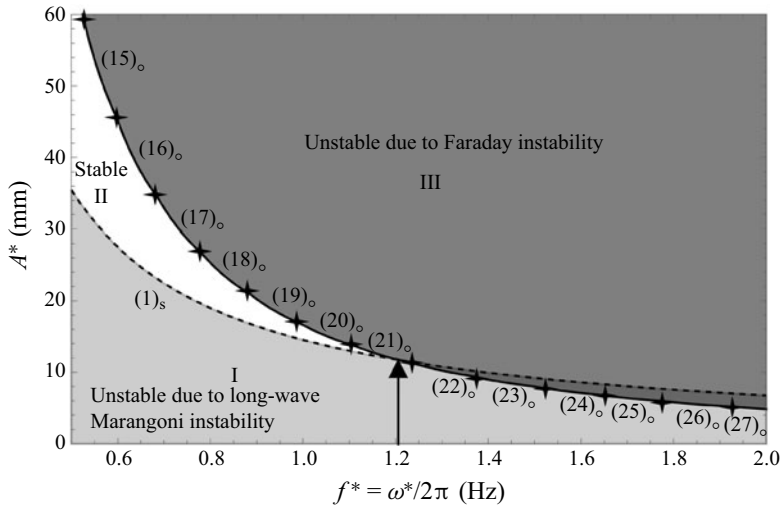
Figure 7. Frequency dependence of the stability bounds for the monotonic (*s*) and oscillatory (*o*) instability modes: $1/W = 0.003$. The A^* versus f^* curves at fixed $Ma = 1.4Ma_c|_{m=1}$ (marked by circle in figure 2*b*). Integers between parentheses, (*m*), identify the most unstable wavenumber $k = 2m\pi/W$. The upward arrow marks the cutoff frequency, where A_o^* becomes equal to A_s^*.

Marangoni number, $Ma > Ma_c$, can render the flow stable. In the current subsection, we investigate whether this holds over a wide frequency range. To this end, we consider a system with physically realizable properties given by table 1, now setting the width to $1/W = 0.003$. The Marangoni number is set to $Ma = 1.4Ma_c$, where Ma_c corresponds to a waveform with $k = 2\pi/W$. This number, $Ma \sim 25$, can be read off the inset of figure 4(*b*). It may be seen from the inset of figure 2(*b*) that for $Ma = 25$, only the waveform corresponding to one wave, i.e. $m = 1$ is unstable, all other allowable waveforms being stable.

Having assigned Ma, we now seek the stability of the flow as we increase the dimensioned forcing amplitude, A^*, until $\sigma_r = 0$, while incrementing the input frequency, f^*. Results are displayed in figure 7, where we once again use dimensioned quantities to emphasize the practical feasibility of the calculations. In this figure, the dashed curve corresponds to the threshold amplitude, A_s^*, required for the stabilization of the monotonic, long-wave Marangoni mode. On this curve, the assigned Ma equals Ma_s. A connection between figures 4 and 7 can be made by considering a frequency of 1 Hz, where the critical amplitude is approximately 15 mm according to figure 7. This corresponds to $\mathcal{A} \sim 0.9\mathcal{A}_c$, i.e. to the intersection of the horizontal and vertical lines in figure 4.

Returning to figure 7, the solid curve represents a second threshold, A_o^*, where the interface deformation is predominantly subharmonic in nature and reflective of resonance. It is here that the assigned $Ma = 1.4Ma_c$ equals Ma_o, as denoted earlier by open circles in figure 5. The integer, m, between parentheses in figure 7 characterizes the most-unstable wavenumber, $k = m2\pi/W$, for a given frequency.

The plot, thus obtained, demarcates three regions of instability/stability, which are separated by the dashed and solid curves. Region I is unstable to a monotonic mode related to the Marangoni instability, region II is fully stable and region III is unstable to a subharmonic oscillatory mode related to Faraday instability.

It should be observed that figure 7 is similar to figure 3(*b*) even though now $Ma \neq 0$. In fact, the numerical values of the critical amplitude, A_o^*, given by the solid lines in the two
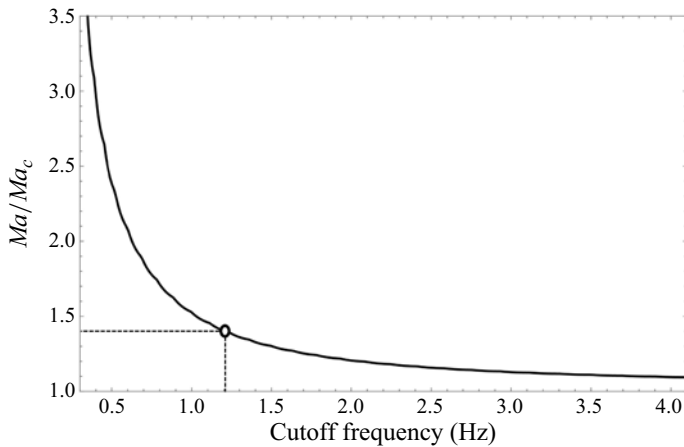
Figure 8. The Ma/Ma_c versus cutoff frequency.

figures are almost indistinguishable from one another. This implies that the Marangoni number has little influence on the onset of resonance, even though the parametric forcing has a strong influence in quenching the Marangoni instability.

Region II exists only in a certain frequency range, until the solid and dashed curves intersect. We designate the frequency, f^*, at the intersection point of the three regions, indicated by the vertical arrow in figure 7, as the cutoff frequency. Beyond this frequency, we move from an unstable Marangoni regime (region I) directly to an unstable resonant regime (region III) eluding any stable transition. Within the thin region between the solid and dashed curves, both the monotonic and oscillatory instability modes grow, but the oscillatory one is dominant. For example, at a forcing frequency of 1.56 Hz, the oscillatory mode with $m = 24$ ought to be observed in an experiment. This means that to the right of the cutoff frequency an increase in amplitude will elicit a drastic change in the modal response from one wave to more than 21 waves. This sudden transition is interpreted from the perspective of A^* versus k curves, in Appendix A.

Let us now consider how the cutoff frequency changes when increasing the assigned Marangoni number. A higher Marangoni number will enhance surface tension gradient flows and to suppress these flows, a higher amplitude of oscillation is required at a given frequency. Hence, the dashed line, which represents the threshold amplitude to quench Marangoni instability, will shift upwards, increasing region I, where the Marangoni instability is dominant and decreasing region II, where the fluid system is stable. This will cause a shift in the cutoff frequency as shown by the graph in figure 8.

The above observations are important as it is known that the pure Marangoni problem in the long-wave region leads to dry spots when the Marangoni number exceeds its critical value (Vanhook *et al.* 1997). To stave off such dry spots with Faraday forcing our calculations would have us hypothesize that we may either force at low frequency leading to a stable flat surface or force at high frequency at the risk of producing large amplitude interfacial oscillatory waves. To check this hypothesis, we proceed to a nonlinear model that allows us to track the interface evolution. This is an involved task but we can gain much insight by appealing to a reduced-order model that uses separation of length scales in the case of thin films, where $\epsilon = 1/W$ is much less than unity. This is done in the next section.

4. Nonlinear computations based on a long-wave model

At large forcing frequencies, linear suppression of the Marangoni instability via parametric forcing, i.e. beyond the dashed curve in figure 7, comes at the price of triggering Faraday waves. In this case, dry spot formation is prevented, which is the minimum requirement for a coating process, but large interface deflections may still occur, thus limiting the surface smoothness of a final coating. In the current section, we investigate whether the nonlinear deflection of the liquid film surface can be minimized nonetheless via a nonlinear interaction between the Marangoni instability and parametric forcing, i.e. below the dashed curve in figure 7.

4.1. *Long-wave approximation*

As we are concerned with the long-wave Marangoni instability mode, we invoke the long-wave approximation, $\epsilon \ll 1$, where $\epsilon = d^*/W^*$ denotes the ratio of normal to transverse length scales (cf. figure 1), in order to derive a low-dimensional WRIBL model, allowing efficient, high-fidelity nonlinear computations (Kalliadasis *et al.* 2011).

We start with the non-dimensional governing equations (2.11)–(2.19), which we truncate at $O(\epsilon^2)$. Thus, both inertia, which plays an important role in parametric instabilities enters at $O(\epsilon)$, and transverse viscous and thermal diffusion, which enter at $O(\epsilon^2)$, are accounted for. We thus obtain the truncated continuity equation

$$\frac{\partial u}{\partial x} + \frac{\partial w}{\partial z} = 0, \tag{4.1}$$

the momentum equations

$$\epsilon Re \left(\frac{\partial u}{\partial t} + u \frac{\partial u}{\partial x} + w \frac{\partial u}{\partial z} \right) = -\epsilon \frac{\partial p}{\partial x} + \epsilon^2 \frac{\partial^2 u}{\partial x^2} + \frac{\partial^2 u}{\partial z^2}, \tag{4.2}$$

$$-\epsilon \frac{\partial p}{\partial z} + \epsilon^2 \frac{\partial^2 w}{\partial z^2} - \epsilon \mathcal{A} \cos(\omega t) = 0 \tag{4.3}$$

and the energy equation

$$\epsilon \left(\frac{\partial T}{\partial t} + u \frac{\partial T}{\partial x} + w \frac{\partial T}{\partial z} \right) = \epsilon^2 \frac{\partial^2 T}{\partial x^2} + \frac{\partial^2 T}{\partial z^2}, \tag{4.4}$$

where we have assumed Re and $\mathcal{A}$ to be of at least $O(\epsilon)$. Further, at $z = h(x, t)$, the interphase coupling conditions are

$$\epsilon \frac{\partial h}{\partial t} = -\epsilon u \frac{\partial h}{\partial x} + \epsilon w, \tag{4.5a}$$

$$\frac{\partial u}{\partial z} \left(1 - \epsilon^2 \left(\frac{\partial h}{\partial x} \right)^2 \right) + \epsilon^2 \frac{\partial w}{\partial x} + 4\epsilon^2 \frac{\partial w}{\partial z} \frac{\partial h}{\partial x} = -\epsilon Ma \left(\frac{\partial T}{\partial x} + \frac{\partial T}{\partial z} \frac{\partial h}{\partial x} \right), \tag{4.5b}$$

$$-\epsilon p + 2\epsilon^2 \left(\frac{\partial w}{\partial z} - \frac{\partial u}{\partial z} \frac{\partial h}{\partial x} \right) = \frac{\epsilon^3}{Ca} \frac{\partial^2 h}{\partial x^2} \tag{4.5c}$$

and

$$Bi(T - T_a) \left[1 + \frac{\epsilon^2}{2} \left(\frac{\partial h}{\partial x} \right)^2 \right] + \frac{\partial T}{\partial z} - \epsilon^2 \frac{\partial T}{\partial x} \frac{\partial h}{\partial x} = 0, \tag{4.5d}$$

where we have assumed the capillary number, Ca, to be at most of $O(\epsilon)$, and the Marangoni number, Ma, to be at least of $O(\epsilon)$. We designate the system of truncated equations given by (4.1)–(4.5) as a $1 + \epsilon^2$ model.

Next, we eliminate the pressure, p, from (4.2) via (4.3) and (4.5c). Integration of (4.3) from z to $z = h(x, t)$, and substitution of (4.5c) for $p|_h$ yields the pressure profile in the liquid film, i.e.

$$\epsilon p|_z = -\frac{\epsilon^3}{Ca}\frac{\partial^2 h}{\partial x^2} + \epsilon\mathcal{A}\cos(\omega t)(h - z) + \epsilon^2\left[\left(\frac{\partial w}{\partial z} - 2\frac{\partial u}{\partial z}\frac{\partial h}{\partial x}\right)\bigg|_h + \frac{\partial w}{\partial z}\bigg|_z\right], \quad (4.6)$$

which is then substituted into (4.2). As a result, we obtain the so-called boundary layer equation governing momentum transport within the liquid film in the long-wave limit, which replaces (4.2) and (4.3)

$$\epsilon Re\left(\frac{\partial u}{\partial t} + u\frac{\partial u}{\partial x} + w\frac{\partial u}{\partial z}\right) = \frac{\epsilon^3}{Ca}\frac{\partial^3 h}{\partial x^3} - \epsilon\mathcal{A}\cos(\omega t)\frac{\partial h}{\partial x} + \frac{\partial^2 u}{\partial z^2} + 2\epsilon^2\frac{\partial^2 u}{\partial x^2}$$

$$+ \epsilon^2\frac{\partial}{\partial x}\left(2\frac{\partial u}{\partial z}\frac{\partial h}{\partial x} - \frac{\partial w}{\partial z}\right)\bigg|_h. \quad (4.7)$$

4.2. *The WRIBL model*

We reduce the dimension of the system of governing equations (4.1), (4.4), (4.5) and (4.7) by eliminating the z-coordinate from the problem and describing the flow in terms of the local instantaneous film surface deflection $h(x, t)$, flow rate $q(x, t)$ and film surface temperature $\theta(x, t)$. This is achieved by integrating (4.4) and (4.7) in the z-direction across the film thickness, i.e. from $z = -1$ to $z = h(x, t)$, following the WRIBL approach (Kalliadasis *et al.* 2011).

First, the dependent variables, u and T, are decomposed into a leading-order contribution (highlighted by a hat) and an $O(\epsilon)$ correction (highlighted by a tilde), i.e.

$$u(x, z, t) = \underbrace{\hat{u}(x, z, t)}_{O(1)} + \underbrace{\tilde{u}(x, z, t)}_{O(\epsilon)}, \quad (4.8)$$

and

$$T(x, z, t) = \underbrace{\hat{T}(x, z, t)}_{O(1)} + \underbrace{\tilde{T}(x, z, t)}_{O(\epsilon)}, \quad (4.9)$$

and w follows from (4.1). For this decomposition to hold, $\hat{u}$ and $\hat{T}$ should remain sufficiently close to the exact solution at all times. This can be achieved by requiring $\hat{u}$ and $\hat{T}$ to satisfy the governing equations (4.1), (4.4), (4.5) and (4.7) truncated at $O(1)$ and by introducing appropriate gauge conditions.

In particular, $\hat{u}$ is governed by the boundary value problem

$$\frac{\partial^2 \hat{u}}{\partial z^2} = K, \quad \hat{u}|_{z=-1} = 0, \quad \text{and} \quad \frac{\partial \hat{u}}{\partial z}\bigg|_{z=h(x,t)} = -\epsilon Ma\left(\frac{\partial \hat{T}}{\partial x} + \frac{\partial \hat{T}}{\partial z}\frac{\partial h}{\partial x}\right), \quad (4.10a\text{–}c)$$

where we have further restricted Ma to be at least of $O(1/\epsilon)$. We have additionally restricted Ca to be at most of $O(\epsilon^3)$, in order to retain the inhomogeneity, K. Further,

we impose the gauge condition,

$$\int_{-1}^{h(x,t)} \hat{u} \, dz = q(x, t), \tag{4.11}$$

which requires that the base velocity profile yield the local instantaneous flow rate $q(x, t)$. Solving (4.10a–c) for $\hat{u}$ subject to (4.11), yields

$$\hat{u} = -\frac{3q(z + 1 - 2(h + 1))(z + 1)}{2(h + 1)^3} - \epsilon Ma \frac{\partial \theta}{\partial x} \frac{(z + 1)(3(z + 1) - 2(h + 1))}{4(h + 1)}, \tag{4.12}$$

which implies for the velocity correction, $\tilde{u}$,

$$\int_{-1}^{h(x,t)} \tilde{u} \, dz = 0, \quad \tilde{u}|_{z=-1} = 0 \quad \text{and} \quad \frac{\partial \tilde{u}}{\partial z}\bigg|_{z=h} = -\left(\epsilon^2 \frac{\partial \hat{w}}{\partial x} + 4\epsilon^2 \frac{\partial \hat{w}}{\partial z} \frac{\partial h}{\partial x}\right). \tag{4.13a–c}$$

Similarly, $\hat{T}$ is governed by the boundary value problem

$$\frac{\partial^2 \hat{T}}{\partial z^2} = 0, \quad \hat{T}|_{z=-1} = 1 \quad \text{and} \quad \hat{T}|_{z=h(x,t)} = \theta, \tag{4.14a–c}$$

where $\theta(x, t)$ is the temperature of the film surface. Solving (4.14a–c) for $\hat{T}$, we obtain

$$\hat{T} = \frac{(\theta - 1)}{h + 1}(z + 1) + 1, \tag{4.15}$$

which implies for the temperature correction, $\tilde{T}$,

$$\tilde{T}|_{z=-1} = 0, \quad \tilde{T}|_{z=h} = 0 \tag{4.16a}$$

and

$$\frac{\partial \tilde{T}}{\partial z}|_{z=h} = -\frac{h + \theta}{h + 1} - Bi\theta + \epsilon^2 \left[\frac{\partial h}{\partial x} \frac{\partial \theta}{\partial x} - \left(\frac{\partial h}{\partial x}\right)^2 \left(\frac{Bi\theta + 1}{2} + \frac{\theta - 1}{h + 1}\right)\right]. \tag{4.16b}$$

Next, we introduce (4.12) and (4.15) in (4.4) and (4.7), truncate the resulting equations at $O(\epsilon^2)$, multiply with the weight functions $F(x, z, t)$ and $\mathcal{W}(x, z, t)$, and integrate across the film height, $1 + h(x, t)$. This yields the integral momentum equation

$$\int_{-1}^{h} \epsilon Re \left(\frac{\partial \hat{u}}{\partial t} + \hat{u} \frac{\partial \hat{u}}{\partial x} + \hat{w} \frac{\partial \hat{u}}{\partial z}\right) F \, dz = \boxed{\int_{-1}^{h} \frac{\partial^2}{\partial z^2}(\hat{u} + \tilde{u}) F \, dz} + \int_{-1}^{h} 2\epsilon^2 \frac{\partial^2 \hat{u}}{\partial x^2} F \, dz$$

$$- \left(\epsilon \mathcal{A} \cos(\omega t) \frac{\partial h}{\partial x} - \frac{\epsilon^3}{Ca} \frac{\partial^3 h}{\partial x^3} - \epsilon^2 \frac{\partial}{\partial x}\left[(2 \frac{\partial \hat{u}}{\partial z} \frac{\partial h}{\partial x} - \frac{\partial \hat{w}}{\partial z})|_h\right]\right) \int_{-1}^{h} F \, dz, \tag{4.17a}$$

and the integral energy equation

$$\int_{-1}^{h} \epsilon \left(\frac{\partial \hat{T}}{\partial t} + \hat{u} \frac{\partial \hat{T}}{\partial x} + \hat{w} \frac{\partial \hat{T}}{\partial z}\right) \mathcal{W} \, dz = \boxed{\int_{-1}^{h} \frac{\partial^2}{\partial z^2}(\hat{T} + \tilde{T}) \mathcal{W} \, dz} + \int_{-1}^{h} \epsilon^2 \frac{\partial^2 \hat{T}}{\partial x^2} \mathcal{W} \, dz, \tag{4.17b}$$

where the unknown corrections, $\tilde{u}$ and $\tilde{T}$, only appear in the boxed terms, expressing wall-normal diffusion. At most other places, $\tilde{u}$ and $\tilde{T}$ drop out due to truncation at $O(\epsilon^2)$.

981 A8-18

Only for the convective terms have we made additional assumptions by dropping the contributions of the corrections, even though $O(\epsilon\tilde{u}) = O(\epsilon\tilde{T}) = O(\epsilon^2)$, implying weak (but finite) inertial and heat convection effects.

The weight functions, F and $\mathcal{W}$, are chosen such as to cancel $\tilde{u}$ and $\tilde{T}$ from the boxed terms in (4.17a) and (4.17b). For F, we require

$$\frac{\partial^2 F}{\partial z^2} = 1, \quad F|_{z=-1} = 0, \quad \left.\frac{\partial F}{\partial z}\right|_{z=h(x,t)} = 0, \tag{4.18a–c}$$

yielding

$$F = \tfrac{1}{2}(z+1)(-2h+z-1), \tag{4.19}$$

and for $\mathcal{W}$, we require

$$\frac{\partial^2 \mathcal{W}}{\partial z^2} = 0, \quad \mathcal{W}|_{z=-1} = 0 \quad \text{and} \quad \left.\frac{\partial \mathcal{W}}{\partial z}\right|_{z=h(x,t)} = \mathcal{C}, \tag{4.20a–c}$$

yielding

$$\mathcal{W} = \mathcal{C}(z+1), \tag{4.21}$$

where $\mathcal{C}$ is an arbitrary constant. Because the weight functions, according to (4.19) and (4.21), correspond to the leading-order profiles $\hat{u}$ (4.12) and $\hat{T}$ (4.15), the weighted integration we have performed corresponds to a Galerkin projection.

As a result of these definitions, the boxed terms in (4.17a) and (4.17b) can be rewritten using integration by parts

$$\int_{-1}^{h} \frac{\partial^2}{\partial z^2}(\hat{u}+\tilde{u})F\,\mathrm{d}z = \left[\frac{\partial(\hat{u}+\tilde{u})}{\partial z}F - (\hat{u}+\tilde{u})\frac{\partial F}{\partial z}\right]_{-1}^{h} + \int_{-1}^{h}(\hat{u}+\tilde{u})\,\mathrm{d}z, \tag{4.22}$$

and

$$\int_{-1}^{h} \frac{\partial^2}{\partial z^2}(\hat{T}+\tilde{T})\mathcal{W}\,\mathrm{d}z = \left[\frac{\partial(\hat{T}+\tilde{T})}{\partial z}\mathcal{W} - (\hat{T}+\tilde{T})\frac{\partial \mathcal{W}}{\partial z}\right]_{-1}^{h}. \tag{4.23}$$

Then, substituting (4.12), (4.13a–c), (4.15), (4.16), (4.19) and (4.21) into (4.17a) and (4.17b), we obtain the final integral momentum and energy equations of our WRIBL model

$$\epsilon Re\left\{\frac{18q^2}{35}\frac{\partial h}{\partial x} - \frac{2\hbar^2}{5}\frac{\partial q}{\partial t} - \frac{34\hbar q}{35}\frac{\partial q}{\partial x}\right\} + \epsilon^2 ReMa\left\{\frac{\hbar^2 q}{56}\left(\frac{3}{2}\hbar\frac{\partial^2\theta}{\partial x^2} + \frac{\partial h}{\partial x}\frac{\partial\theta}{\partial x}\right)\right.$$

$$\left. + \frac{\hbar^3}{120}\left(\hbar\frac{\partial^2\theta}{\partial x\partial t} + \frac{19}{7}\frac{\partial\theta}{\partial x}\frac{\partial q}{\partial x}\right)\right\} - \epsilon^3 ReMa^2\frac{\hbar^4}{336}\frac{\partial\theta}{\partial x}\left\{\frac{19}{5}\frac{\partial h}{\partial x}\frac{\partial\theta}{\partial x} + \frac{5}{2}\hbar\frac{\partial^2\theta}{\partial x^2}\right\}$$

$$= q + \frac{\hbar^3}{3}\left\{\epsilon A\frac{\partial h}{\partial x}\cos(\omega t) - \frac{\epsilon^3}{Ca}\frac{\partial^3 h}{\partial x^3}\right\} + \epsilon Ma\frac{\hbar^2}{2}\frac{\partial\theta}{\partial x}$$

$$+ \epsilon^2\left\{\frac{9\hbar}{5}\left(\frac{\partial h}{\partial x}\frac{\partial q}{\partial x} - \frac{\partial^2 q}{\partial x^2}\hbar\right) + \frac{4q}{5}\left(3\hbar\frac{\partial^2 h}{\partial x^2} - 2\left(\frac{\partial h}{\partial x}\right)^2\right)\right\}$$

$$+ \epsilon^3 Ma\hbar^2\left\{\frac{\hbar}{10}(3\frac{\partial^2\theta}{\partial x^2}\frac{\partial h}{\partial x} + \frac{\partial^3\theta}{\partial x^3}\hbar) + \frac{1}{15}\frac{\partial^2 h}{\partial x^2}\frac{\partial\theta}{\partial x}\hbar - \frac{4}{5}\frac{\partial\theta}{\partial x}\left(\frac{\partial h}{\partial x}\right)^2\right\}, \tag{4.24a}$$

and

$$\epsilon \left\{ \frac{1}{3}\hbar^2 \frac{\partial \theta}{\partial t} + \frac{7}{120}\hbar \frac{\partial q}{\partial x}(\theta - 1) + \frac{9}{20}\hbar q \frac{\partial \theta}{\partial x} \right\}$$

$$+ \frac{\epsilon^2 Ma\hbar^2}{40}\left[(1 - \theta)\left(\frac{1}{2}\frac{\partial \theta^2}{\partial x^2}\hbar + \frac{\partial h}{\partial x}\frac{\partial \theta}{\partial x} \right) - \hbar\left(\frac{\partial \theta}{\partial x} \right)^2 \right] = 1 - \theta - \hbar(Bi\theta + 1)$$

$$- \epsilon^2 \hbar \left\{ \frac{(Bi\theta + 1)}{2}\left(\frac{\partial h}{\partial x} \right)^2 - \frac{1}{3}\frac{\partial^2 \theta}{\partial x^2}\hbar + \frac{(\theta - 1)}{3}\left(\frac{\partial^2 h}{\partial x^2} + \frac{1}{\hbar}\left(\frac{\partial h}{\partial x} \right)^2 \right) - \frac{1}{3}\frac{\partial h}{\partial x}\frac{\partial \theta}{\partial x} \right\},$$

$$(4.24b)$$

where we have substituted $\hbar = 1 + h$. These equations are completed by the integral continuity equation

$$\frac{\partial h}{\partial t} + \frac{\partial q}{\partial x} = 0, \qquad (4.24c)$$

obtained by integrating (4.1) from $z = -1$ to $z = h(x, t)$, and invoking the interphase mass balance (4.5a). Thus, our final model (4.24) consists of a nonlinear system of three evolution equations in terms of the three unknowns $h(x, t)$, $q(x, t)$ and $\theta(x, t)$.

Observe that (4.24a) contains a mixed derivative, $\partial_{xt}\theta$, at one place. The latter appears as a result of the base velocity profile $\hat{u}$ chosen in (4.12), and, in particular, as a result of retaining the leading-order Marangoni stress in the boundary condition (4.10a–c). We find that this choice greatly improves the linear stability predictions of our model. Neither in the linear stability calculations nor in the nonlinear computations (where we use a spectral method for spatial discretization) do the mixed derivative pose any numerical challenge.

4.3. *Numerical procedure*

Numerically, to solve the system of nonlinear equations, (4.24), we discretize variables in space along the horizontal direction using a Fourier spectral scheme (Hesthaven, Gottlieb & Gottlieb 2007). This automatically satisfies periodicity in the *x*-direction, which is the setting considered in the current manuscript. In all our nonlinear computations, the domain length is set to the container width, *W*. Time integration is realized via the NDSolve function in Mathematica (version 12.1). Each of our nonlinear computations is started from an initial perturbation constructed with the eigenfunctions $h'|_{t=0}$, $q'|_{t=0}$, and $\theta'|_{t=0}$, defined according to (3.2), and obtained from a preliminary linear stability calculation for $\mathcal{A} = 0$ and $Ma > Ma_c$. The initial deflection amplitude was set to be 5 % of the fluid depth. The grid resolution for our simulations was determined via grid independence tests by a stepwise doubling of the number of collocation points until the change in the minimum interface deflection, $h_{min}(t)$, was less than 1 %.

4.4. *Nonlinear suppression of dry spots*

To validate our long-wave model (4.24), we start by reproducing the neutral stability bounds from figure 7. For this, we linearly perturb the dependent variables $h(x, t)$, $q(x, t)$ and $\theta(x, t)$ according to (3.2), and solve the resulting eigenvalue problem to obtain the critical forcing amplitude, $\mathcal{A}$, at fixed ω, Ma and $\epsilon = 0.003$, using the parameters in table 1. Results are represented in figure 9, where, as in figure 7, the dashed curve represents the monotonic instability mode ($\hat{h}_0 \gg \hat{h}_n$ for all $n \neq 0$) and the solid curve
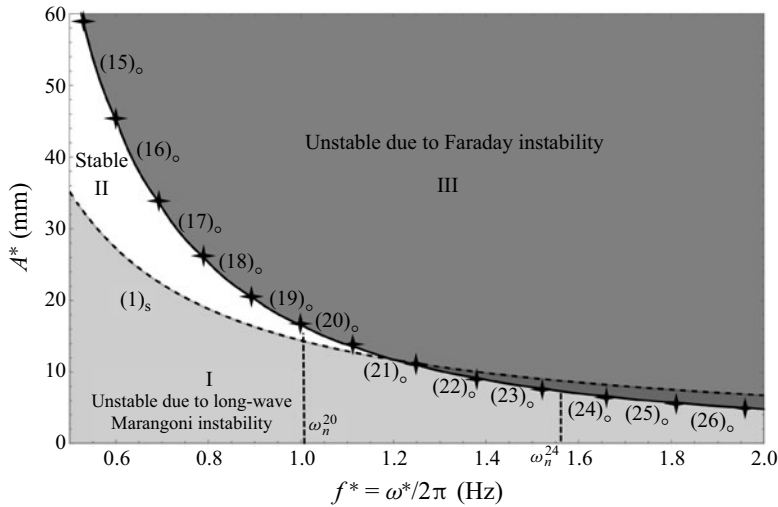
Figure 9. Linear effect of parametric forcing on Marangoni instability, as predicted by the long-wave model (4.24). Critical forcing amplitude A^* versus forcing frequency f^*. The same parameters as in figure 7: $d^* = 3$ mm; $\epsilon = d^*/W^* = 0.003$; $Ma = 1.4Ma_c|_{k=2\pi}$. Dashed curve, stability bound of monotonic mode ($\hat{h}_0 \gg \hat{h}_n$ for all $n \neq 0$); solid curve, stability bound for oscillatory modes ($\hat{h}_n \gg \hat{h}_0$ for at least one $n \neq 0$). Numbers (m) designate wavenumber $k = 2m\pi$ of critical spatial mode. For the chosen parameters, only $m = 1$ yields an unstable Marangoni mode at $A^* = 0$.

represents the oscillatory instability mode ($\hat{h}_n \gg \hat{h}_0$ for at least one $n \neq 0$). Agreement with the corresponding curves in figure 7 is excellent, due to the smallness of the chosen $\epsilon = 0.003$, which warrants the long-wave approximation underlying our model.

We next perform nonlinear computations based on (4.24) for parameters lying in the three characteristic regions of figure 9. In region I, the liquid film is always unstable to a Marangoni mode with $m = 1$, i.e. $k = 2\pi$. Recall that, in this section, the wavenumber, k, is scaled by the container width, W^*, i.e. $k = k^*W^*$. In region II, the film is rendered linearly stable via parametric forcing. In region III, the film is always unstable to Faraday waves.

Figure 10 represents the time evolution of the film thickness profile, $\hbar = 1 + h(x, t)$, in the limit $A^* = 0$, where only the Marangoni instability is active. The value of the Marangoni number is $Ma = 1.4Ma_c|_{k=2\pi} = 25$. Here $k = 2\pi$ is the only possible instability mode (cf. figure 2b), as a result of our choice for the container width, i.e. $\epsilon = 0.003$. It is observed that the deflection of the film surface increases as time progresses, until the liquid–gas interface at the trough reaches the lower wall. The film surface buckles, forming two secondary troughs, which drastically slow down further draining of liquid from the trough region. As shown by Boos & Thess (1999) and Dietze, Picardo & Narayanan (2018), additional buckling events may follow (at higher Ma), but, eventually, the liquid film will always rupture due to spinodal dewetting (Bonn *et al.* 2009). Thus, it is safe to say that the nonlinear evolution in figure 10, will lead to the formation of a dry spot, in accordance with the experimental observations of Vanhook *et al.* (1997) for very thin liquid films. Supplementary movie 1 shows the evolution towards dry spot formation in action.

We now consider how the nonlinear evolution in figure 10 is altered by applying additional parametric forcing with increasing forcing amplitude, A^*. For this, we consider two forcing frequencies, i.e. $f^* = 1$ Hz, which corresponds to the natural frequency at
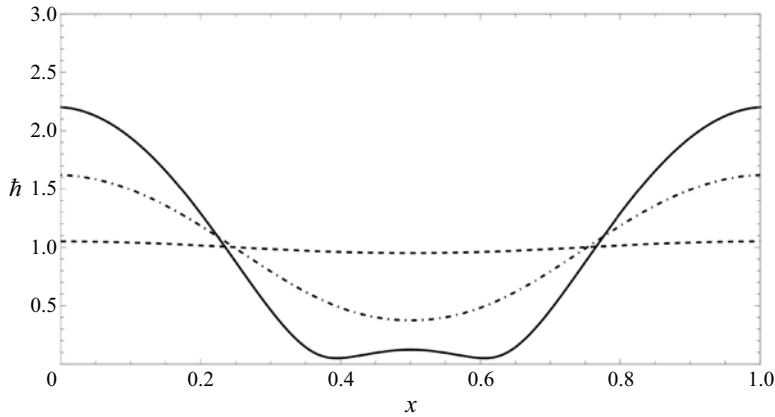
Figure 10. Nonlinear computation for parameters according to region I in figure 9: $A^* = 0$; $Ma = 25$. Interface profile of dry spot formation at different times t. Dashed curve, $t = 0$; dashed-dotted curve, $t = 7$; solid curve, $t = 14$. See also Supplementary movie 1, available at https://doi.org/10.1017/jfm.2024.58.
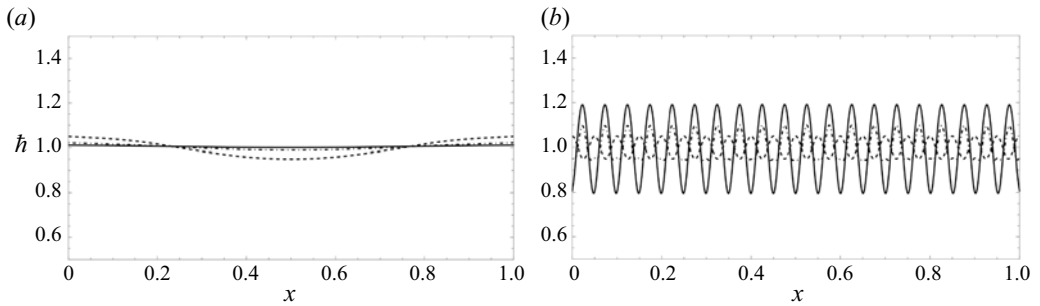

Figure 11. Nonlinear effect of parametric forcing on Marangoni instability. Numerical computations with WRIBL model (4.24), showing transition from regions II to III in figure 9: $f^* = 1$ Hz; $Ma = 1.4Ma_c|_{k=2\pi}$. Film surface profiles at different times t: dashed curves, $t = 0$. (a) Linear suppression of surface deformations: $A^* = 0.9A_c^*$ (region II in figure 9). Dash–dotted curve, $t = 45$; solid curve, $t = 90$. (b) Saturated Faraday waves: $A^* = 1.1A_c^*$ (region III of figure 9). Dashed-dotted curve, $t = 0.001$; solid curve, $t = 0.002$. See also Supplementary movies 2 and 3. Here A_c^* corresponds to solid curve in figure 9.

$m = 20$, and $f^* = 1.56$ Hz, which corresponds to the natural frequency at $m = 24$. We start by discussing our computations for $f^* = 1$ Hz which are represented in figure 11. At $A^* = 0.9A_c^*$ (figure 11a), parameters lie in region II of figure 9, and our nonlinear computation indicates a full attenuation of the initial interface deflection. Thus, parametric forcing indeed allows us to obtain a perfectly flat film surface in this parameter range. Supplementary movie 2 shows the evolution towards flatness in action.

When the forcing amplitude is increased to $A^* = 1.1A_c^*$, which lies in region III of figure 9, Faraday waves appear. Here, the resonant action takes over and the interface develops $m = 20$ waves per container width, as shown in figure 11(b). Although dry spot formation is still prevented under these conditions, we see that large interface deflections result from the parametric forcing. Supplementary movie 3 shows the formation of resonant waves in action.

A different picture emerges for the higher forcing frequency, $f^* = 1.56$ Hz, as shown in figure 12. It is known from figure 9 that linear stabilization of the liquid film cannot be achieved under these conditions, as the solid curve for the onset of oscillatory instability
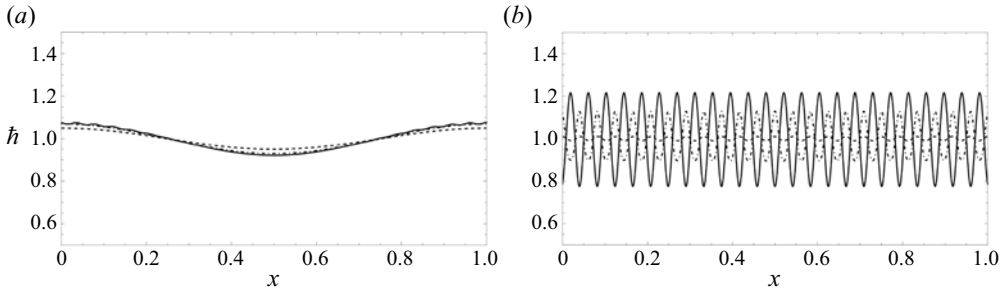
Figure 12. Nonlinear effect of parametric forcing on Marangoni instability. Numerical computations with WRIBL model (4.24), showing transition from regions I to III in figure 9: $f^* = 1.56$ Hz; $Ma = 1.4Ma_c|_{k=2\pi}$. Film surface profiles at different times t: dashed curves, $t = 0$. (*a*) Nonlinear attenuation of surface deformations: $A^* = 0.9A_c^*$ (region I in figure 9). Dash–dotted curve, $t = 2$; solid curve, $t = 3.5$. (*b*) Saturated Faraday waves: $A^* = 1.1A_c^*$ (region III in figure 9). Dashed–dotted curve, $t = 0.001$; solid curve, $t = 0.002$. See also Supplementary movies 4 and 5.
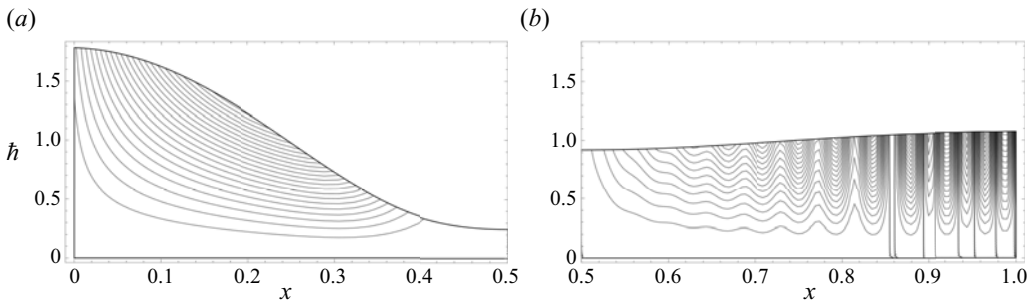

Figure 13. Change in flow structure within the liquid film. Streamlines in the laboratory reference frame for parameters corresponding to figure 10 and figure 12(*a*). (*a*) Dry spot formation (figure 10): $A^* = 0.1A_c^*$; $Ma = 1.4Ma_c|_{k=2\pi}$; and $f = 1.56$ Hz. (*b*) Nonlinear saturation due to parametric forcing (figure 12*a*): $A^* = 0.9A_c^*$; $Ma = 1.4Ma_c|_{k=2\pi}$; and $f^* = 1.56$ Hz. Only one half of the domain is represented in each panel, for convenience.

lies below the dashed curve demarcating stabilization of the monotonic instability mode. Nonetheless, figure 12(*a*) shows evidence of a very strong nonlinear saturation of the interface deflection at $A^* = 0.9A_c^*$, even though this point lies in region I of figure 9. Here, the interface remains almost flat, notwithstanding that it is subject to the long-wave Marangoni instability mode, responsible for forming dry spots in the absence of forcing. Thus, dry spot formation can be prevented and the film can be rendered virtually flat also at higher forcing frequencies, albeit due to a nonlinear mechanism (figure 12*a*), in contrast to the linear mechanism observed at low frequencies (figure 11*a*).

This nonlinear saturation mechanism is associated with small standing waves or ripples forming on the main humps of the interface deformation. These are only slightly visible in figure 12(*a*), but their oscillatory motion can be distinguished clearly in the Supplementary movie 4. These standing waves or ripples form at the main humps or crests rather than the main troughs on account of the inertial action promoted by the height of fluid below the large deflecting crests. We believe that these standing waves are responsible for arresting further drainage of liquid from the deformation trough, as a result of a cellular flow pattern that develops underneath the deformation hump. This is seen in figure 13, which displays streamlines in the laboratory reference frame for the two cases from figures 10 and 12(*a*).
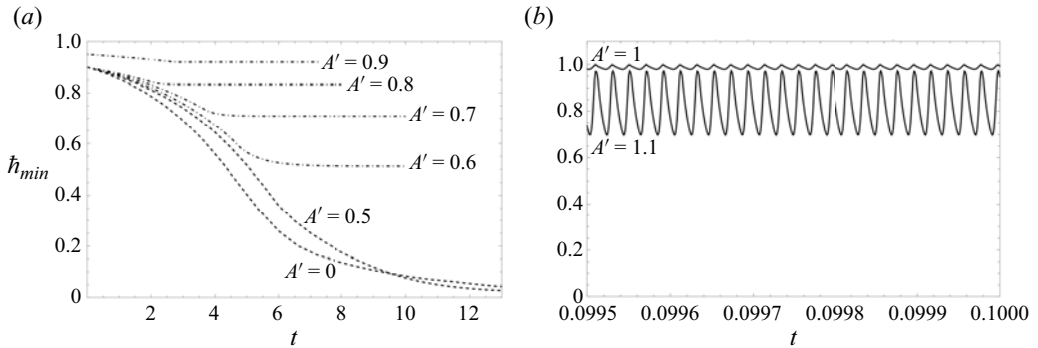
Figure 14. Effect of relative forcing amplitude $A' = A^*/A_c^*$ on long-time nonlinear evolution of the heated liquid film. Parameters according to figure 9: $f^* = 1.56$ Hz. Time traces of the minimum film thickness $\hbar_{min} = 1 + h_{min}$. (*a*) Nonlinear attenuation of surface deformation in region I of figure 9: $A' < 1$. From bottom to top: $A' = 0, 0.5, 0.6, 0.7, 0.8$ and 0.9. (*b*) Saturated Faraday waves: $A' \geq 1$. From bottom to top: $A' = 1.1$ and 1.

Finally, we turn to figure 12(*b*), which shows that the nonlinear saturation of the surface deformation is lost, when the forcing amplitude is increased to $A^* = 1.1A_c^*$, where large-amplitude short Faraday waves form once again, as a result of oscillatory instability (see also Supplementary movie 5).

From an application point of view, one may ask at what forcing amplitude, A^*, does the nonlinear saturation of the interface deflection set in? We have quantified this for the current parameters in figure 14, which represents time traces of the minimum film thickness, $\hbar_{min} = 1 + h_{min}$, for different subcritical (figure 14*a*) and supercritical (figure 14*b*) forcing amplitudes A^*, all other parameters remaining the same as in figure 12. Based on figure 14(*a*), we may conclude that a significant nonlinear attenuation of the interface deflection is achieved for $A^*/A_c^* \geq 0.7$.

5. Summary

The interaction of parametric forcing and Marangoni instability is viewed from two perspectives. In the first perspective, we use linear stability analysis to conclude that parametric forcing will stabilize long-wave Marangoni instability but has little effect on short-wave Marangoni-driven waveforms. It is seen that a layer unstable to Marangoni flows may be completely stabilized by parametric forcing at low frequencies but becomes unstable to resonant waves at high amplitudes of forcing. However, at higher parametric frequencies, the fluid system directly transitions from an unstable Marangoni regime to an unstable resonant regime, thus circumventing the transition to a stable state.

In a second perspective, validation of the results of linear stability was done using a reduced-order nonlinear model that tracked the interface evolution in the presence of parametric forcing over a range of frequencies. In addition to recovering the results forecast by linear stability, this model shows that, at frequencies beyond a critical value, the resonant forcing subverts the subcritical nature of the long-wave nonlinear Marangoni instability, constraining the interface to a low-amplitude saturated form. This nonlinear saturation mechanism is due to the formation of vortices underneath the choppy Faraday waves excited by the parametric forcing. The vortices arising from these Faraday waves disrupt the thermocapillary flow that drains liquid from the global trough to the global hump. In some ways, this is similar to the suppression of dry spots by the short-wave Marangoni instability mode (Vanhook *et al.* 1997).

981 A8-24

As it is known from experiments that long-wave Marangoni instability will lead to dry spots, we conclude that a major outcome of this study is that the evolution of the interface can be suppressed at both low and high frequencies, preventing dry-out.

Our observations were made for the case where gravity is absent. We conclude by assessing the effect of finite gravity. A finite gravitational acceleration, g, acts on the large interface deflections and thereby stabilizes the long-wave Marangoni instability. Therefore, incrementing the value of g for the calculation in figure 4(*a*) would shift the threshold of the long-wave Marangoni instability mode upwards, eventually leading it to surpass the minimum threshold of the short-wave mode (itself insensitive to gravity). It is below this limit, that the formation of dry spots is possible; and, in this regime, we find that the long-wave Marangoni instability mode remains highly sensitive to parametric forcing.

Author ORCIDs.
- I.B. Ignatius https://orcid.org/0009-0005-7930-7615;
- B. Dinesh https://orcid.org/0000-0002-4883-1554;
- G.F. Dietze https://orcid.org/0000-0003-1495-5505;
- R. Narayanan https://orcid.org/0000-0003-2394-5077.

Appendix A. Supplement to figure 7: role of the wavenumber

In this appendix, we discuss the origin and implications of the cutoff frequency, $f^* \sim$ 1.2 Hz, observed in figure 7, where the stability bounds of the monotonic and oscillatory instability modes intersect. To do this, the spatial confinement imposed by the finiteness of the container width, W, needs to be considered. We then represent the stability bounds in terms of A^* versus k curves for the parameters used in figure 7. These curves, depicted in figure 15, are drawn for two values of the forcing frequency, f^*, i.e. $f^* = 1$ Hz (diamonds) and $f^* = 1.56$ Hz (circles), which are situated on either side of the cutoff frequency. Dashed curves correspond to the monotonic and solid curves to the oscillatory instability modes. Figure 15(*a*) shows both bounds in the same diagram, while a magnified view of the monotonic instability bound, which is confined to a narrow wavenumber range, is provided in figure 15(*b*). Note that the flow is unstable, when $A^* = 0$, to all wavenumbers less than k_c denoted on figure 15(*b*) by an upward arrow. Likewise the system is quiescent for all allowable wavenumbers greater than k_c.

As a result of the fixed container width, $1/W = 0.003$, there is only one allowable unstable wavenumber, $k = 2\,m\pi/W$, for the monotonic mode at the considered $Ma = 1.4Ma_c|_{k=2\pi/W}$. This waveform, given by $m = 1$, is marked by a vertical line in figure 15(*b*). At the corresponding wave number, the monotonic Marangoni instability mode can be suppressed by increasing the forcing amplitude, A^*, e.g. beyond the filled diamond in figure 15(*b*) for a forcing frequency of $f^* = 1$ Hz. Observe that this value of A^*, denoted A_s^* is less than A_o^*, the lowest amplitude for the allowable wavenumbers on the oscillatory curve. Upon increasing the frequency to $f^* = 1.56$ Hz, the oscillatory curves shift substantially, while the monotonic curves shift only slightly. This shift in the oscillatory curves with frequency is characteristic of resonant instabilities (cf. Kumar & Tuckerman 1994; Batson, Zoueshtiagh & Narayanan 2013). The critical amplitude,
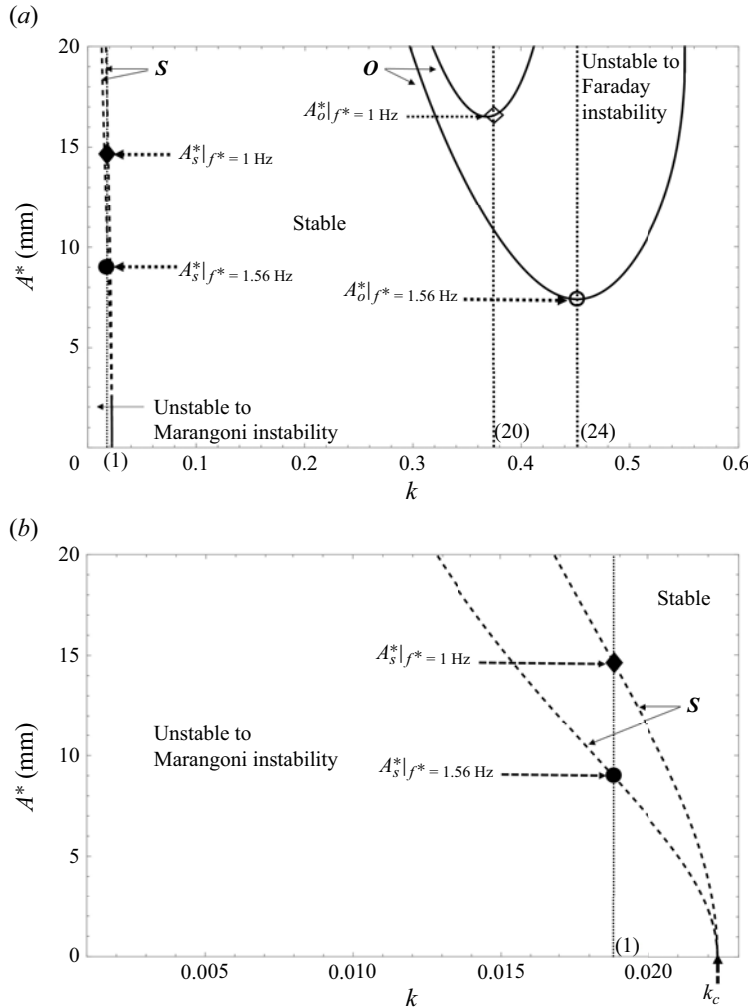
Figure 15. Effect of forcing frequency on the most unstable allowable waveforms and associated critical forcing amplitude for the monotonic (s) and oscillatory (o) instability modes. Critical A^* versus k curves for two frequencies from figure 7: $Ma = 1.4 Ma_c|_{k=2\pi/W}$; $1/W = 0.003$. Diamonds, $f^* = 1$ Hz; circles, $f^* = 1.56$ Hz. Dotted vertical lines mark most-unstable allowable waveforms, identified by $m = Wk/2\pi$ (given between parentheses). Panel (b) is a magnified view of the long-wave range in panel (a).

A_o^*, diminishes with increasing forcing frequency (from open diamond to open circle in figure 15a), and does so at a greater rate than the stability bound of the monotonic mode (figure 15b). Consequently, the oscillatory instability bound eventually moves below the monotonic stability bound, implying the existence of a cutoff frequency, as observed in figure 7.

To see the effect of lateral confinement of the container, we observe that the allowable wavenumbers along the monotonic curve shift to the left with increase in container width. Likewise, the allowable wavenumbers in the oscillatory curve shift towards the minimum with increase in container width. This implies that there is a critical width for which $A_s^* = A_o^*$ for a fixed parametric frequency, f^*. Below this width, unstable Marangoni flow can be completely stabilized. Above this width, the Marangoni instability transitions to

981 A8-26

resonant waves with an increase in forcing amplitude. Consequently, at fixed supercritical *Ma*, stabilization cannot be achieved in the unconfined case, no matter how large the forcing amplitude. A finite container width is thus a prerequisite for the existence of the dashed curve in figure 7.

In summary, there are two prerequisites for the occurrence of a cutoff frequency. First, the coexistence of monotonic and oscillatory instability modes, and, second, a finite lateral confinement. We point out that these prerequisites can be satisfied also by other interfacial instability problems. For example, critical A^* versus k curves similar to figure 15 are seen in parametric stabilization of Rayleigh–Taylor instability (Sterman-Cohen *et al.* 2017). Therefore, one might expect to obtain a regime diagram similar to figure 7 also in that case.

Appendix B. Effect of an active upper air layer

The stability calculations reported in the main body of this manuscript rely on assuming a hydrodynamically passive and purely conducting upper fluid layer. In this appendix, we assess the validity of this assumption by checking how an active upper gas layer, such as air, affects the stability bounds represented in figure 7. That figure contains several of our key findings related to the effect of parametric forcing on the Marangoni instability.

The additional stability calculations are performed based on the full governing equations in the liquid film and upper air layer, following Smith (1966) and Kumar & Tuckerman (1994). The standard properties of air (subscript a) at ambient pressure and temperature are used. Further, the air-to-liquid depth ratio is set to $d_a^*/d^* = 2$, which follows from the value of $Bi = \mathcal{H}d^*/\lambda = 0.1$ used throughout the study, assuming $\mathcal{H} = \lambda_a/d_a^*$. The results of the calculations are presented in figure 16, where all other parameters correspond to figure 7. The differences between figures 16 and 7 are extremely small, less than 1 %, which warrants the assumption of a hydrodynamically passive and purely conducting upper gas layer.

The weak effect of the upper air layer on our key observations results from the low density and viscosity of air. As a result of this, the upper layer cannot meaningfully affect the inertia-driven Faraday instability and the inertia-driven stabilization of the long-wave Marangoni instability, which dictate the thresholds represented in figures 7 and 16.

Appendix C. Validity of the long-wave approximation underlying the WRIBL model

Figures 12 and 13(*b*) show evidence of shorter choppy waves and associated vortices within the liquid film. The question may arise as to whether the long-wave approximation underlying our WRIBL model is still valid for these regimes. The horizontal length scale of the said structures is dictated by the wavelength, Λ^*, of the most-amplified Faraday mode, which is quantified via the number between parentheses in figure 9, i.e. the number of waves, $m = W^*/\Lambda^*$, within the container width W^*. Thus, we evaluate the maximal length scale ratio, $\epsilon_{max} = d^*/\Lambda^* = \epsilon m$, based on the wavelength of the Faraday waves in figure 12, where $m = 24$. This yields $\epsilon_{max} \sim 0.1$, which is generally small enough for an $O(\epsilon^2)$ long-wave WRIBL model, such as ours, to yield accurate predictions.

We demonstrate this for our specific configuration by comparing the linear stability predictions obtained with our WRIBL model with predictions based on the full governing equations. First, we compare the stability bounds in figure 9, which are obtained from our WRIBL model, with those in figure 7, which are obtained from the full governing equations. The stability bounds are in good agreement and only differ by less than 1 %.
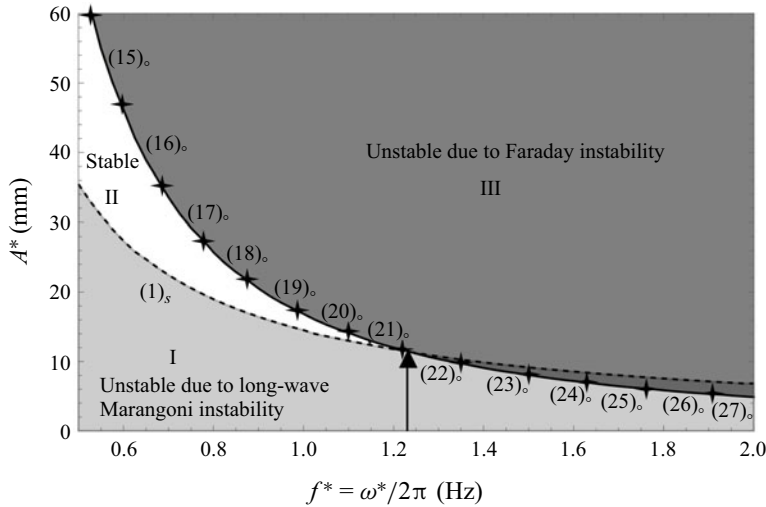
Figure 16. Neutral stability bounds according to figure 7 for the case of an active upper air layer, as obtained from calculations based on the full governing equations in the liquid and air, following Smith (1966). Air parameters: $d_a^*/d^* = 2$; $\rho_a = 1$ kg m^{-3}; $\mu_a = 1.6 \times 10^{-5}$ Pa s; $\lambda_a = 0.026$ W m^{-1} K^{-1}; $C_{pa} = 1$ J kg^{-1} K^{-1}. The air-to-liquid depth ratio, $d_a^*/d^* = 2$, follows from the value of $Bi = \mathcal{H}d^*/\lambda = (\lambda_a d^*)/(\lambda d_a^*) = 0.1$ used in figure 7. All other parameters according to figure 7: $Ma = 1.4 Ma_c|_{k=2\pi/W}$; $1/W = 0.003$.
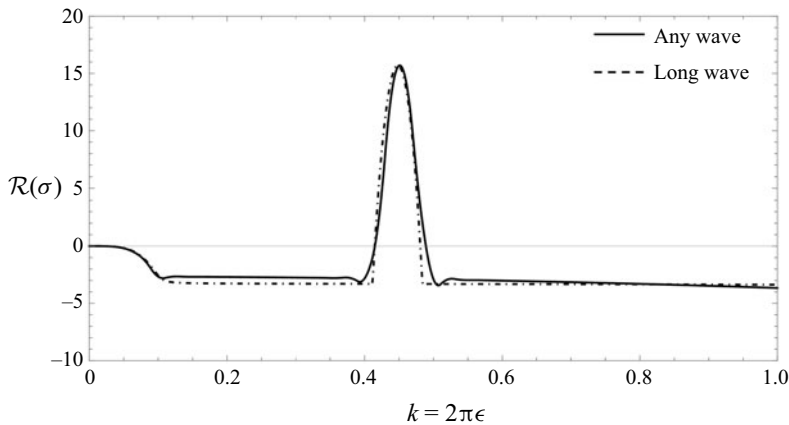

Figure 17. Validation of the WRIBL model versus linear stability calculations based on the full governing equations. Growth rate dispersion curves for the parameters in figure 12(b): $f^* = 1.56$ Hz; $Ma = 1.4 Ma_c|_{m=1}$, where $m = 1$ corresponds to the first allowable wavenumber. Solid curve, full governing equations; dot–dashed curve, WRIBL model.

Second, we compare the growth rate curves (figure 17) obtained with the two approaches for the parameters in figure 12(b). We again observe very good agreement over the entire relevant range of the wavenumber, k, including and far beyond the most-amplified wavenumber, which prevails in our nonlinear calculations (figure 12b).

REFERENCES

AJAEV, V.S. 2013 Instability and rupture of thin liquid films on solid substrates. *Interfacial. Phenom. Heat Transfer* **1** (1).

ALEXEEV, A., GAMBARYAN-ROISMAN, T. & STEPHAN, P. 2005 Marangoni convection and heat transfer in thin liquid films on heated walls with topography: experiments and numerical study. *Phys. Fluids* **17** (6), 062106.

BATSON, W., ZOUESHTIAGH, F. & NARAYANAN, R. 2013 The Faraday threshold in small cylinders and the sidewall non-ideality. *J. Fluid Mech.* **729**, 496–523.

BONN, D., EGGERS, J., INDEKEU, J., MEUNIER, J. & ROLLEY, E. 2009 Wetting and spreading. *Rev. Mod. Phys.* **81** (2), 739–805.

BOOS, W. & THESS, A. 1999 Cascade of structures in long-wavelength Marangoni instability. *Phys. Fluids* **11** (6), 1484–1494.

BRISKMAN, V. 1996 Vibrational control of interface stability. In *34th Aerospace Sciences Meeting and Exhibit*, AIAA 96-0595, 1-10.

DAVIS, S.H. 1987 Thermocapillary instabilities. *Annu. Rev. Fluid Mech.* **19** (1), 403–435.

DIETZE, G.F., PICARDO, J.R. & NARAYANAN, R. 2018 Sliding instability of draining fluid films. *J. Fluid Mech.* **857**, 111–141.

FARADAY, M. 1831 On a peculiar class of acoustical figures; and on certain forms assumed by groups of particles upon vibrating elastic surfaces. *Phil. Trans. R. Soc. Lond.* **121**. doi:10.1098/rstl.1831.0018.

FAYZRAKHMANOVA, I.S. & NEPOMNYASHCHY, A.A. 2018 Vibration influence on the onset of the longwave Marangoni instability in two-layer system. *Phys. Fluids* **30** (2), 024104.

GOTTLIEB, O. & ORON, A. 2004 Stability and bifurcations of parametrically excited thin liquid films. *Intl J. Bifurcation Chaos* **14** (12), 4117–4141.

GRESHO, P.M. & SANI, R.L. 1970 The effects of gravity modulation on the stability of a heated fluid layer. *J. Fluid Mech.* **40** (4), 783–806.

GRODZKA, P.G. & BANNISTER, T.C. 1972 Heat flow and convection demonstration experiments aboard apollo 14. *Science* **176** (4034), 506–508.

GUO, W., LABROSSE, G. & NARAYANAN, R. 2013 *The Application of the Chebyshev-Spectral Method in Transport Phenomena*. Springer Science & Business Media.

HAIMOVICH, O. & ORON, A. 2010 Nonlinear dynamics of a thin liquid film on an axially oscillating cylindrical surface. *Phys. Fluids* **22** (3), 032101.

HALPERN, D. & GROTBERG, J.B. 2003 Nonlinear saturation of the rayleigh-instability due to oscillatory flow in a liquid-lined tube. *J. Fluid Mech.* **492**, 251–270.

HESTHAVEN, J.S., GOTTLIEB, S. & GOTTLIEB, D. 2007 *Spectral Methods for Time-Dependent Problems*. Cambridge University Press.

KALLIADASIS, S., RUYER-QUIL, C., SCHEID, B. & VELARDE, M.G. 2011 *Falling Liquid Films*. Springer Science & Business Media.

KAMOTANI, Y., OSTRACH, S. & PLINE, A. 1995 A thermocapillary convection experiment in microgravity. *J. Heat Transfer* **117** (3), 611–618.

KOSCHMIEDER, E.L. 1993 *Bénard Cells and Taylor Vortices*. Cambridge University Press.

KUMAR, K. & TUCKERMAN, L.S. 1994 Parametric instability of the interface between two fluids. *J. Fluid Mech.* **279**, 49–68.

LEE, Y.S. & FARSON, D.F. 2016 Surface tension-powered build dimension control in laser additive manufacturing process. *Intl J. Adv. Manuf. Technol.* **85**, 1035–1044.

MURRAY, B.T., MCFADDEN, G.B. & & CORIELL, S.R. 1990 Stabilization of Taylor–Couette flow due to time-periodic outer cylinder oscillation. *Phys. Fluids* A*: Fluid Dyn.* **2** (12), 2147–2156.

NAYFEH, A.H. 1981 *Perturbation Techniques*. John Wiley & Sons.

NEPOMNYASHCHY, A.A. & SIMANOVSKII, I.B. 2010 Long-wave Marangoni convection in two-layer films under the action of gravity modulation. *Microgravity. Sci. Technol.* **22** (3), 265–271.

NEPOMNYASHCHY, A.A. & SIMANOVSKII, I.B. 2013 The influence of vibration on Marangoni waves in two-layer films. *J. Fluid Mech.* **726**, 476–496.

NIELD, D.A. 1964 Surface tension and buoyancy effects in cellular convection. *J. Fluid Mech.* **19** (3), 341–352.

ORON, A., DAVIS, S.H. & BANKOFF, S.G. 1997 Long-scale evolution of thin liquid films. *Rev. Mod. Phys.* **69** (3), 931.

PEARSON, J.R.A. 1958 On convection cells induced by surface tension. *J. Fluid Mech.* **4** (5), 489–500.

RUYER-QUIL, C. & MANNEVILLE, P. 2000 Improved modeling of flows down inclined planes. *Eur. Phys. J.* B*-Condens. Matt. Complex Syst.* **15** (2), 357–369.

SARMA, G.S.R. 1987 Interaction of surface-tension and buoyancy mechanisms in horizontal liquid layers. *J. Thermophys. Heat Transfer* **1** (2), 129–135.

SCRIVEN, L.E. & STERNLING, C.V. 1964 On cellular convection driven by surface-tension gradients: effects of mean surface tension and surface viscosity. *J. Fluid Mech.* **19** (3), 321–340.

SHKLYAEV, S., ALABUZHEV, A.A. & KHENNER, M. 2015 Marangoni convection in a thin film on a vertically oscillating plate. *Phys. Rev.* E **92** (1), 013019.

SHUKLA, P.K. & NARAYANAN, R. 2002 The effect of time-dependent gravity with multiple frequencies on the thermal convective stability of a fluid layer. *Intl J. Heat Mass Transfer* **45**, 4011–4020.

SKARDA, J.R.L. 2001 Instability of a gravity-modulated fluid layer with surface tension variation. *J. Fluid Mech.* **434**, 243–271.

SMITH, K.A. 1966 On convective instability induced by surface-tension gradients. *J. Fluid Mech.* **24** (2), 401–414.

STEPHENSON, A. 1908 On induced stability. *Lond. Edinb. Dublin Phil. Mag. J. Sci.* **15** (86), 233–236.

STERMAN-COHEN, E., BESTEHORN, M. & ORON, A. 2017 Rayleigh–Taylor instability in thin liquid films subjected to harmonic vibration. *Phys. Fluids* **29**, 052105.

THIELE, U., VEGA, J.M. & KNOBLOCH, E. 2006 Long-wave Marangoni instability with vibration. *J. Fluid Mech.* **546**, 61–87.

VANHOOK, S.J., SCHATZ, M.F., SWIFT, J.B., McCORMICK, W.D. & SWINNEY, H.L. 1997 Long-wavelength surface-tension-driven Bénard convection: experiment and theory. *J. Fluid Mech.* **345**, 45–78.

YIANTSIOS, S.G. & HIGGINS, B.G. 2006 Marangoni flows during drying of colloidal films. *Phys. Fluids* **18** (8), 0821031.